Next Energy 12 (2026) 100645

Contents lists available at ScienceDirect

Next Energy

journal homepage: www.sciencedirect.com/journal/next-energy

Research article

Device-level simulation of lead-free perovskite solar cells ($MASnI_3$, $MASnBr_3$, and $MABiI_3$): A comparative study using SCAPS-1D

M.A.A. Fahad[a], M.M. Islam[b], S. Mahmud[b,*], S. Narjim[c], S. Shanta[a], M.T. Khatun[d], M.M. Alam[a,e,**]

[a] Department of Electrical and Electronic Engineering, Islamic University, Kushtia 7003, Bangladesh
[b] Department of Electrical and Electronic Engineering, Jatiya Kabi Kazi Nazrul Islam University (JKKNIU), Mymensingh 2224, Bangladesh
[c] Department of Electrical and Electronic Engineering, Pabna University of Science and Technology, Pabna, Bangladesh
[d] Atomic Energy Centre Dhaka, Bangladesh Atomic Energy Commission, Dhaka 1000, Bangladesh
[e] Hamdard University Bangladesh, Hamdard Nagar, Gazaria, Munshiganj 1510, Bangladesh

ARTICLE INFO

Keywords:
Perovskite
HTL ($CsSnI_3$)
ETL (SnO_2)
$MASnI_3$
Quantum efficiency
Solar cell

ABSTRACT

Perovskite solar cells (PSCs) based on lead have achieved a record power conversion efficiency (PCE) in recent years; however, the toxicity and stability of Pb, especially of $CH_3NH_3PbI_3$, limits its commercialization. As a result, much effort is being put into developing lead-free PSCs. This paper compares the performances of different types of lead-free PSCs and their choice of absorber materials using Solar Cell Capacitance Simulator-1D simulations. In this context, the use of $MASnI_3$, $MASnBr_3$, and $MABiI_3$ as solvent-processed absorbers and their effects on Voc, Jsc, fill factor, and PCE are discussed in this part of the study snippets series. $MASnI_3$ shows the best comprehensive cell efficiency with a maximum PCE of 30.04%. Similarly, $MASnBr_3$ and $MABiI_3$ deliver high performance, with maximum PCEs of 29.19% and 27.97%, respectively, obtained at optimized absorber thicknesses. The outcomes demonstrate the effect of the thickness of the absorber layer, the doping concentration, and the defect density on the performance of the device, revealing that the device with $MASnI_3$ has proved superior performance under the above parameters. Additionally, it elaborates on the enhancement strategies for the hole transport layer and electron transport layer, propagating the idea that defect density at interfaces must be minimized. This study contributes to the ongoing efforts to make highly efficient, lead-free PSCs a practical reality while aiding in sustainable energy conversion and storage.

1. Introduction

The growing exhaustion of fossil fuels and the increasing environmental impact of their utilization have led to global attention to renewable energy sources [1]. Solar energy has proven to be one of the most promising alternatives to combat climate change and achieve sustainability in the energy sector [2–5]. Perovskite solar cells (PSCs) are a promising photovoltaic technology that has gained widespread interest because of their unique advantages in efficiency, cost, and the possibility to prepare them in a simple wet chemistry process [6–8]. The performance of PSCs has risen drastically over just a decade, establishing PSCs as a fierce competitor to the commonly used silicon-based photovoltaic cells [9]. They mark a turning point in the development of solar energy technologies, and PSCs are now seen as one of the most favorable candidates for future commercial solar power generation.

PSCs are considered the third generation of thin-film photovoltaic technologies [10,11]. Based on organic-inorganic metal halide perovskite semiconductors, these devices have several intrinsic advantages over classical silicon-based solar cells. Their tunable band gaps, high absorption coefficients, low exciton binding energies, and potential for solution-based processing techniques underpin the importance of their discovery [12]. For these factors, the power conversion efficiency (PCE) of PSCs has developed by leaps and bounds over the past few years, going from an initial 3.8% (2009) to contacts of almost 25%, thus exceeding a large set of other sorts of thin-film solar cells in viability [13–16]. The scalability of perovskite-based devices also positions them as an appealing solution for large-scale solar power applications, enabling widespread electricity generation.

The structure of PSCs is defined by the ABX_3 general formula [17], where X represents a halogen ion such as Cl^-, Br^-, or I^-, A can be either formamidinium ($CHNH_3^+ = NH$) ion or an organic species like

* Corresponding author.
** Corresponding author at: Hamdard University Bangladesh, Hamdard Nagar, Gazaria, Munshiganj 1510, Bangladesh.
E-mail addresses: shuaib.eee.iu@gmail.com, shuaibmahmud@jkkniu.edu.bd (S. Mahmud), monjarul@hamdarduniversity.edu.bd (M.M. Alam).

https://doi.org/10.1016/j.nxener.2026.100645
Received 19 February 2026; Received in revised form 7 April 2026; Accepted 10 April 2026

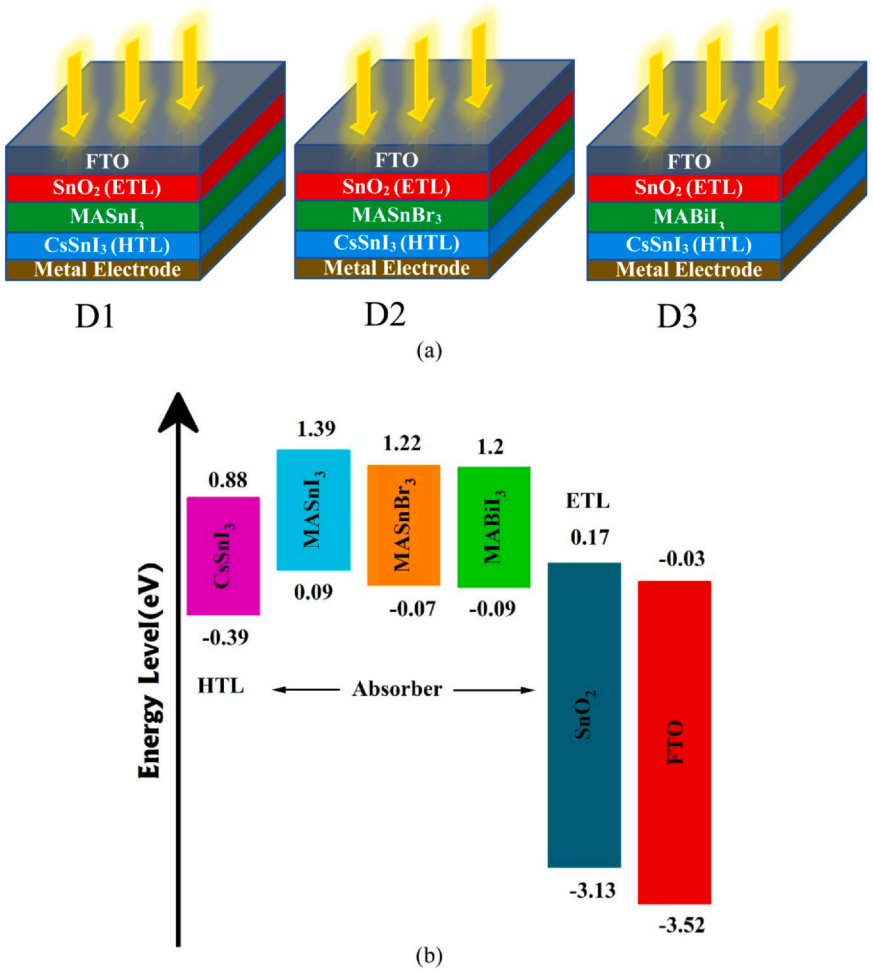

Fig. 1. (a) Initial device structures (b) Energy band diagram. ETL = electron transport layer; HTL = hole transport layer.

Table 1
Initial simulation parameters of the studied perovskite solar cells

Properties	Absorbers			HTL	ETL	FTO
	$MASnI_3$	$MASnBr_3$	$MABiI_3$	$CsSnI_3$	SnO_2	
t [μm]	0.5	0.5	0.5	0.35	0.03	0.4
E_g [eV]	1.3	1.3	1.3	1.27	3.3	3.5
X_e [eV]	4.17	4.17	4.17	4.47	4	4
ϵ_r	8.2	10	6.5	18	9	9
N_C (cm^{-3})	1×10^{18}	2.2×10^{18}	1×10^{18}	1.58×10^{19}	2.2×10^{17}	2.2×10^{18}
N_V (cm^{-3})	1×10^{18}	1.8×10^{18}	1×10^{19}	1.47×10^{18}	2.2×10^{16}	1.8×10^{18}
μ_e(cm^2 Vs^{-1})	1.6	1.6	1.6	4.37	200	20
μ_h (cm^2 Vs^{-1})	1.6	1.6	1.6	4.37	80	10
N_D (cm^{-3})	0	0	0	0	1×10^{17}	1×10^{19}
N_A (cm^{-3})	3.2×10^{15}	1×10^{18}	3.2×10^{13}	1×10^{19}	0	0
N_t (cm^{-3})	1×10^{15}	1×10^{14}	1×10^{14}	1×10^{14}	1×10^{15}	1×10^{14}
Ref.	[40]	[20]	[41]	[34]	[20]	[42]

Where, t = thickness, E_g = band gap, X_e = electron affinity, E_r = relative dielectric; N_c, N_v = state densities of conduction and valence band; μ_n, μ_h = electron and hole mobility; N_D, N_A, N_t = density of donor, acceptor, and defect, respectively; ETL = electron transport layer; HTL = hole transport layer.

Table 2
Input parameters of HTL/perovskite and perovskite/ETL interface defect layers [43]

Parameter	HTL/Perovskite	Perovskite/ETL	ETL/FTO
Defect density	Neutral	Neutral	Neutral
Electron capture cross section (cm^2)	1.0×10^{-19}	1.0×10^{-19}	1.0×10^{-19}
Hole capture cross section (cm^2)	1.0×10^{-19}	1.0×10^{-19}	1.0×10^{-19}
Energetic distribution	Single	Single	Single

ETL = electron transport layer; HTL = hole transport layer.

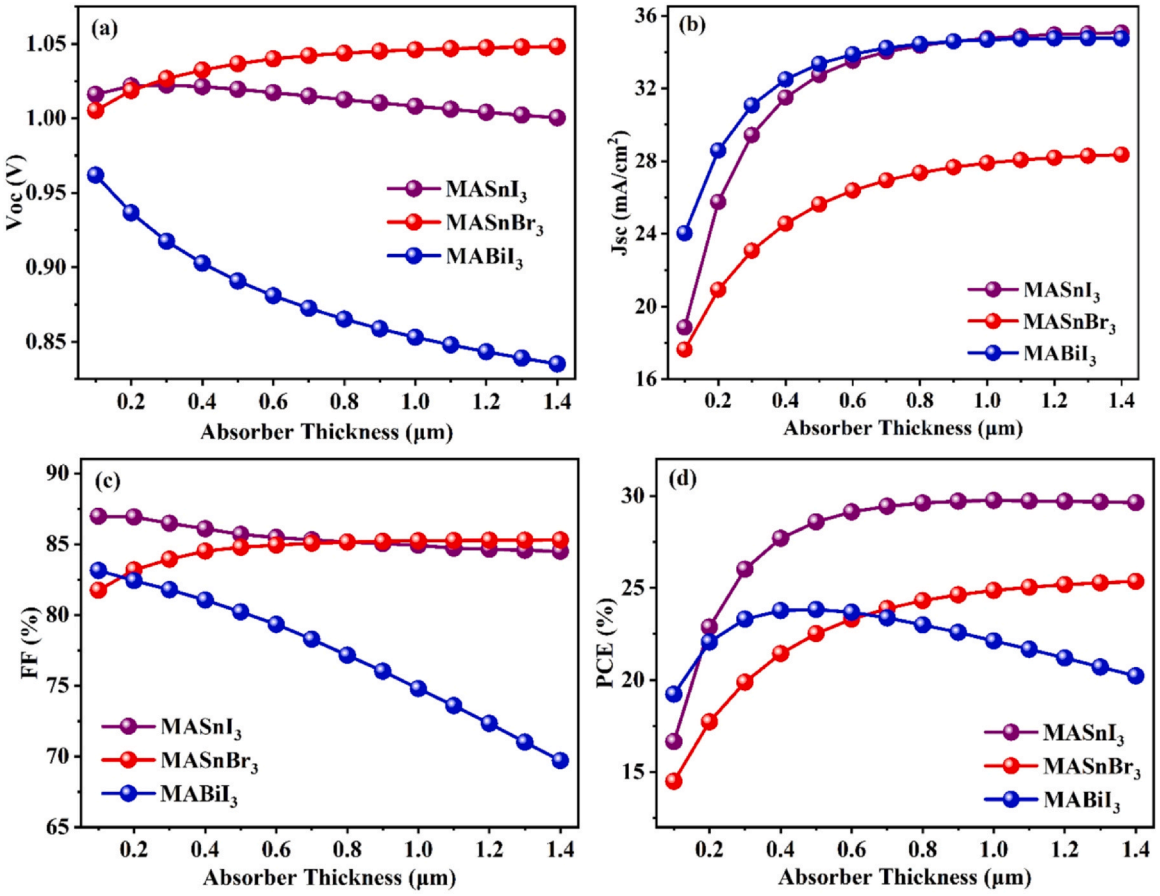

Fig. 2. Variations in the performance of the PSC based on alterations in the thickness of the perovskite layer. (a) V_{oc}; (b) J_{sc}; (c) FF; (d) PCE. FF = fill factor; J_{sc} = short-circuit current density; PCE = power conversion efficiency; PSC = perovskite solar cell; V_{oc} = open-circuit voltage.

methyl ammonium ($CH_3NH_3^+$) ion, and B is an inorganic cation such as Sn^{2+} or Pb^{2+}. While methyl ammonium lead iodide ($MAPbI_3$) has been widely utilized as an absorber material in PSCs [18], its adoption is constrained due to the hazardous nature of lead. Consequently, alternative materials involving tin (Sn) or bismuth (Bi) have been investigated as substitutes to mitigate environmental concerns and enhance the sustainability of PSC technology [16,19,20]. Although PSCs show promise to be efficient in converting light into electricity, the commercial potential of this technology is currently stunted by multiple challenges, with stability posing one of the biggest objections to large-scale deployment. Despite their great photo conversion efficiency, the stability of perovskite materials in the presence of moisture, heat, oxygen, and ultraviolet (UV) radiation is still an open issue for the PSC commercial application [21]. Lead-free PSCs, particularly those based on tin and bismuth, show significant commercial potential with promising efficiency and stability, positioning them as viable candidates for large-scale solar energy applications [22–25].

In particular, the perovskite layer itself is susceptible to degradation due to environmental issues, which can result in the rapid loss of performance of the overall solar cell. Hence, comprehending and tackling the stability of PSCs at the level of the absorber layer, as well as the complete device structure, is of utmost importance for the real practical success of these devices. Besides the inherent vulnerability of the perovskite material itself, interfaces between these layers (the perovskite absorber, hole transport layer [HTL], and electron transport layer [ETL]) of the device can lead to performance losses and instability [26]. Therefore, a comprehensive investigation should be conducted to improve the stability of PSCs and discover materials that are capable of tolerating environmental stresses while retaining high performance [27].

The optimization of PSCs is not limited to the selection of the absorber material. Desired high-efficiency requirements of these devices involve the utilization of effective HTLs and ETLs to efficiently extract charge carriers from the perovskite absorber layer. HTLs and ETLs are pivotal in determining the device performance because they transport holes and electrons to their corresponding electrodes. It is critical to choose these transport layers since this choice will not only maximize efficiency but will also help to stabilize the device. Conventional HTLs (e.g., 2,2′,7,7′-Tetrakis(N,N-di-p-methoxyphenylamine)-9,9′-spirobifluorene and Poly(3,4-ethylenedioxythiophene):Poly(styrenesulfonate)) are principally employed in PSCs; however, they are confronted with challenges in terms of process cost, stability, and scalability [28,29]. Consequently, candidate materials for the HTL are being explored, inclusding alternative materials, such as cesium tin iodide ($CsSnI_3$). For large-scale production of PSCs, these materials provide stability and cost benefits, which are major considerations [30]. The ETL material also plays a significant role, as ETL material is also critical for performance and stability. Mesoporous TiO_2 has been the most widely used ETL for PSCs because of its good electron-transporting properties and excellent stability. TiO_2, on the other hand, needs to be processed at high temperatures, hindering the fabrication process and curbing low-cost scaling potential. Furthermore, TiO_2-based PSCs have shown instability under UV irradiation and prolonged forward bias conditions, which have affected the device performance in the long run [31]. Consequently, the focus of researchers has shifted towards other promising n-type wide band gap semiconductors, such as SnO_2, ZnO, WO_3, etc., which can be processed at lower temperatures and demonstrate better stability under operational conditions. This is especially significant for lead-free and eco-friendly Sn-PSCs, since alternative dopant-free ETLs and HTLs can be developed to avoid using toxic

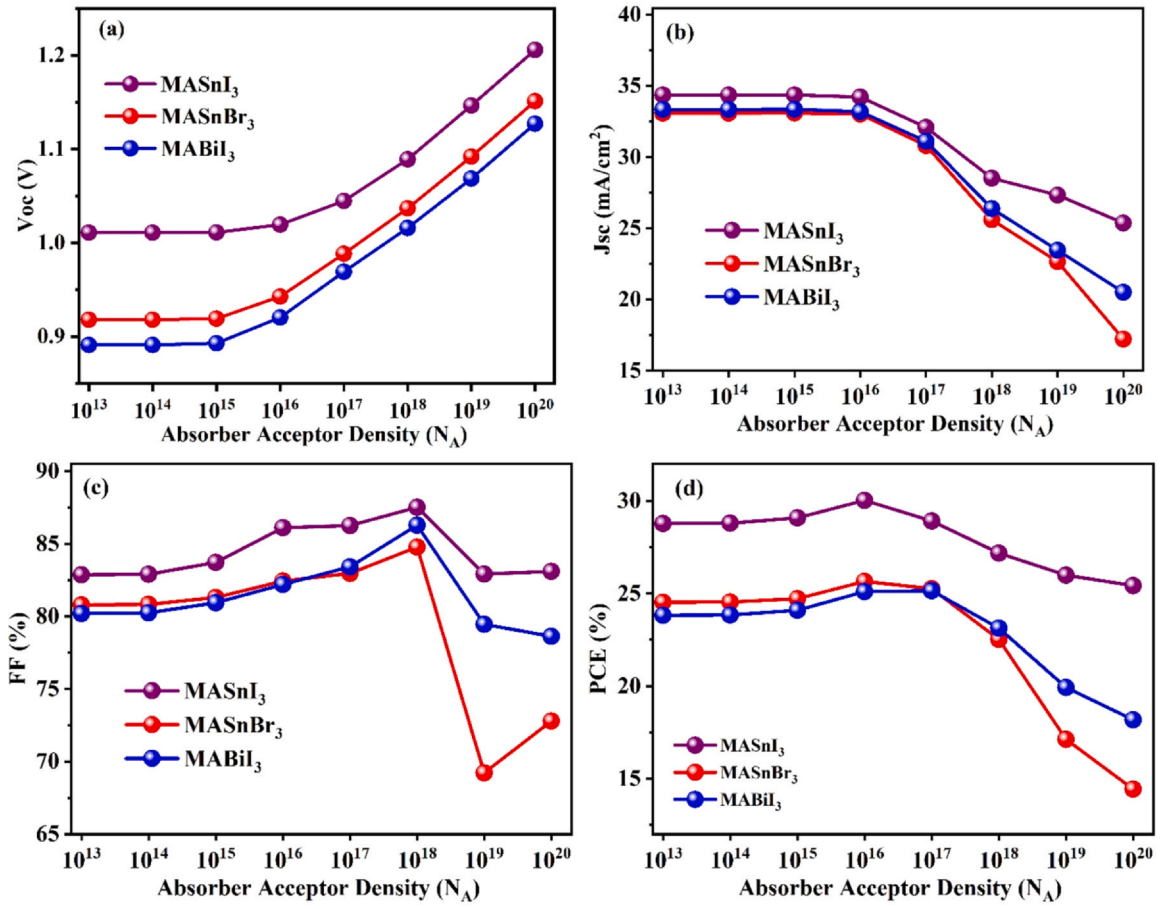

Fig. 3. Variations in the performance of the PSC based on alterations in the acceptor density of the perovskite layer. (a) V_{oc}; (b) J_{sc}; (c) FF; (d) PCE. FF = fill factor; J_{sc} = short-circuit current density; PCE = power conversion efficiency; PSC = perovskite solar cell; V_{oc} = open-circuit voltage.

materials that are present in classical ETLs and HTLs (e.g., nitrogen and phosphorous doped thin films of TiO_2 and NiO in comparison to lead-based alternatives [32]. SnO_2 is one of the most promising ETLs to date for optoelectronic properties, low-temperature processes, and high performance in this context. SnO_2-based PSCs have shown great promise for attaining high PCEs and for overcoming the toxicity issues of lead-based materials [33]. $CsSnI_3$ has emerged as a potential alternative as the HTL due to its inherent stability and efficiency as a tin-based perovskite material over the more traditional carbon HTLs. Additionally, using $CsSnI_3$ increases the stability of the device with better hole extraction efficiency [34].

To further enhance the performance of Sn-PSCs, a systematic study of the influence of the different device parameters, including the thickness, doping concentration, and defect density of the absorber layer, and the doping concentration and thickness of the transport layers, is critical. We model and simulate the performance of a tin/bismuth-based PSC in this study using the Solar Cell Capacitance Simulator (SCAPS-1D). $CH_3NH_3SnI_3$/ $CH_3NH_3SnBr_3$/$CH_3NH_3BiI_3$, SnO_2, and $CsSnI_3$ are used as absorbers, ETLs, and HTLs, respectively, in a realistic device configuration simulation. It enables the examination of various device parameters in order to improve the device's solar cell performance and stability.

This study is novel in that it presents a direct comparative analysis of $MASnI_3$, $MASnBr_3$, and $MABiI_3$ lead-free perovskite absorbers under an identical device architecture, which provides a benign and green alternative to lead-based solar cells. While previous studies have predominantly focused on individual materials, there is a lack of comprehensive studies that evaluate and compare these materials under similar conditions. This will be an important step for future solar-engineering technologies, as this will be a means by which studied PSCs can meet the increasing demand for renewable energy in a sustainable fashion.

2. Methodology

2.1. Simulation tool

Thorough numerical simulations of the PSC structures were conducted using the SCAPS-1D simulation tool, developed by the Department of Electronics and Information Systems at the University of Gent, Belgium. This versatile tool is widely employed for simulating various solar cell types, including perovskite, CdTe-based, and silicon-based solar cells. Capable of modeling up to 7 layers in a single-cell structure, the software facilitates the adjustment of solar cell parameters such as band gap, defect density, doping, and thickness [35]. The SCAPS program utilizes Poisson's equation, establishing the connection between photo-carriers and the electrostatic potential within the semiconductor. Additionally, it employs continuity equations to depict the kinetics of charge generation and recombination in materials [36]. The solution to both Poisson's equation and the continuity equation provides insight into the quantum efficiency (QE) and current-voltage (J–V) characteristics [37]. By employing Poisson's equation and the continuity equation, one can deduce the electron and hole densities [38]. Furthermore, Poisson's equation allows for the determination of the electric field distribution, denoted as E(x):

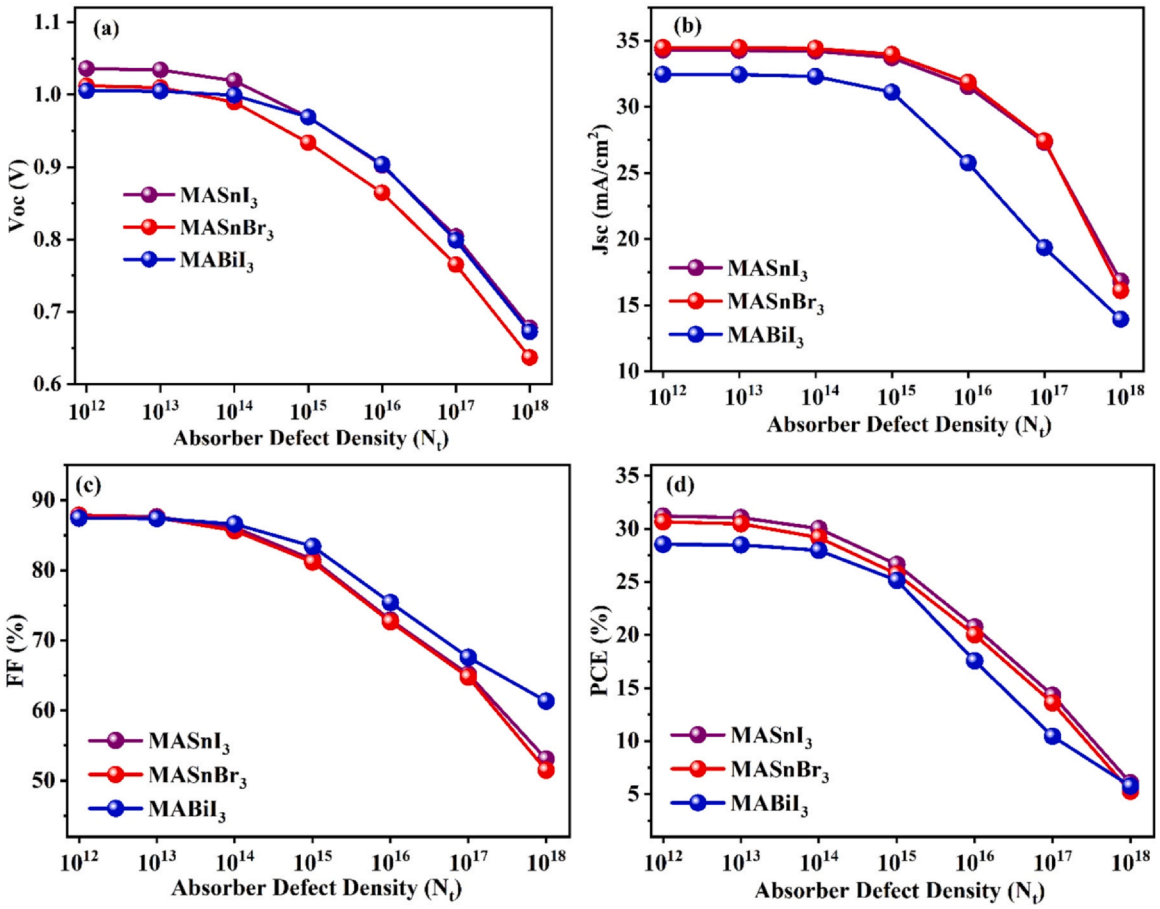

Fig. 4. Variations in the performance of the PSC based on alterations in the defect density of the perovskite layer. (a) V_{oc}; (b) J_{sc}; (c) FF; (d) PCE. FF = fill factor; J_{sc} = short-circuit current density; PCE = power conversion efficiency; PSC = perovskite solar cell; V_{oc} = open-circuit voltage.

$$\frac{dE}{dx} = \frac{\rho}{\varepsilon}, \quad \rho(x) = q(N_D + p - N_A - n)$$

Drift and diffusion current densities play a pivotal role in governing the transport characteristics of charge carriers within a semiconductor. The ensuing equations delineate the expressions for both drift and diffusion current densities pertaining to electrons and holes [39].

$$J_n = qn(x)\mu_n E(x) + qD_n \frac{dn}{dx}$$

$$J_p = qp(x)\mu_p E(x) - qD_p \frac{dp}{dx}$$

Where, μ_n and μ_p = electron and hole mobility, ε = dielectric permittivity, $\rho(x)$ = the space charge distribution, q = charge of an electron, D_n and D_p = the diffusion coefficients of electrons and holes, $n(x)$ and J_n = the concentration and current density of electrons, $p(x)$ and J_p = the concentration and current density of holes.

All simulations were performed under standard AM1.5 G solar illumination with an incident power density of 1000 W/m^2 at a temperature of 300 K. The boundary conditions for the simulation assumed ideal contact interfaces. The SCAPS-1D simulation assumes one-dimensional carrier transport under steady-state conditions.

2.2. Device structure

The device structure consists of FTO/SnO_2/Perovskite/$CsSnI_3$/Ni (5.35 eV), where SnO_2 acts as the ETL and $CsSnI_3$ serves as the HTL. The energy band alignment between these layers enables efficient electron extraction through the ETL and hole extraction through the HTL, while reducing interfacial recombination losses. Proper alignment of conduction and valence bands ensures improved charge separation and overall device performance. The simulated PSCs are analyzed based on their device structures, as illustrated in Fig. 1(a) and energy level of all layer is shown in Fig. 1(b). This study explores 3 distinct device configurations, labeled as D1, D2, and D3, for simulation purposes. The relevant simulation data is summarized in Table 1 and the input parameters of HTL/Perovskite and Perovskite/ETL interface defect layers presented in Table 2.

3. Results and discussion

3.1. Optimization of absorber

The perovskite layer, which creates charge carriers by absorbing light, determines the PSC performance. Several factors, such as thickness, doping concentration, defect density, etc., of the absorber layer affect the performance of PSC [44]. In this study, 3 distinct absorber layers, namely $MASnI_3$, $MASnBr_3$, and $MABiI_3$ ($MA = CH_3NH_3^+$), have been optimized.

3.1.1. Thickness optimization

The thickness of the perovskite layer plays a crucial role in governing the spread and duration of photo-generated holes and electrons. Achieving an optimal absorber layer thickness is essential for

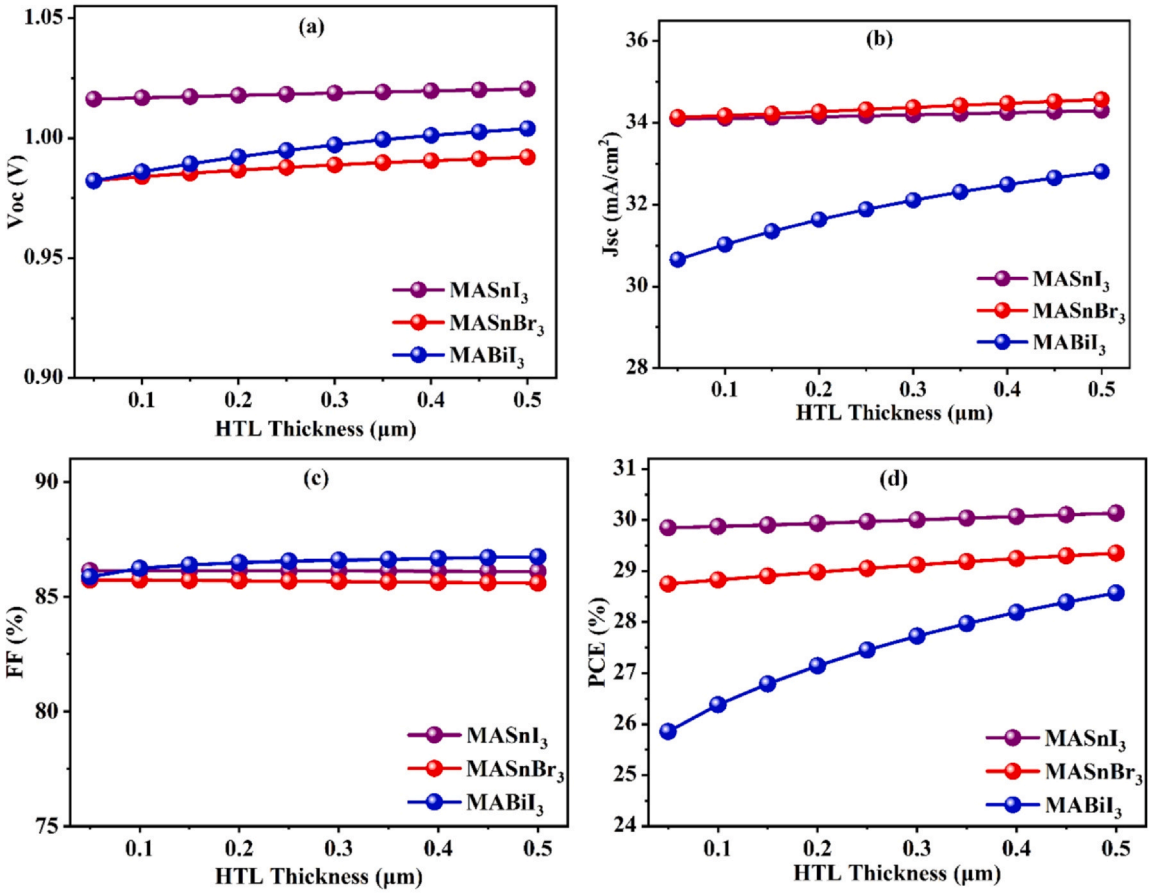

Fig. 5. Variation of HTL thickness on (a) V_{oc}; (b) J_{sc}; (c) FF; (d) PCE. FF = fill factor; HTL = hole transport layer; J_{sc} = short-circuit current density; PCE = power conversion efficiency; V_{oc} = open-circuit voltage.

maximizing photon absorption and generating electron-hole pairs effectively [45]. To investigate the effect of perovskite layer thickness on the performance of PSCs, the thicknesses of $MABiI_3$, $MASnBr_3$, and $MASnI_3$ were varied from 0.1 μm to 1.4 μm. The open-circuit voltage (Voc) of $MASnI_3$ varies slightly with the absorber layer thickness, from 1.02 V at 0.10 μm to 1 V at 1.40 μm. In comparison, however, $MASnBr_3$ has consistent Voc values, beginning at 1.01 V (0.10 μm) and rising marginally to 1.05 V (1.40 μm). Comparatively, $MABiI_3$ exhibits the lowest Voc ranges from 0.96 V at 0.10 μm to 0.84 V at 1.40 μm position in Fig. 2 (a), which implies $MABiI_3$ is less effective in retaining voltage with increasing absorber layer thickness and therefore, is also the least stable candidate for the Voc. In Fig. 2(b), the short-circuit current density (J_{sc}) of $MASnI_3$ increases distinctly with the increase of absorber layer thickness, showing a peak value of 35.07 mA/cm^2 at 1.40 μm compared to 18.85 mA/cm^2 at 0.10 μm, indicating that $MASnI_3$ is good at producing photo-generated current for thicker absorber layer thicknesses. $MASnBr_3$ displays a similar trend, where Jsc ranges from 17.64 mA/cm^2 at 0.10 μm to 28.36 mA/cm^2 at 1.40 μm; however, the values are lower than $MASnI_3$ along the range. Jsc (24.04 mA/cm^2 at 0.10 μm – 34.75 mA/cm^2 at 1.40 μm) also rises for $MABiI_3$, but $MASnI_3$ has a higher Jsc than the other 2 giving indicates $MABiI_3$ has lower performance in current generation concurrently with increasing thickness.

It is worth noting that the fill factor (FF) of $MASnI_3$ is very high (86.97% for 0.10 μm and 84.51% for 1.40 μm) in Fig. 2(c), indicating that $MASnI_3$ could maintain good efficiency in terms of charge carrier collection and overall device performance with a lower thickness of the absorber layer. On the other hand, while the FF of $MASnBr_3$ is improved from 81.75% at 0.10 μm to 85.29% at 1.40 μm, it suggests that this material will achieve higher throughput even if the thickness of the absorber is increased. The FF of $MABiI_3$ decreased the most, going from 83.14% at 0.10 μm to 69.71% at 1.40 μm with the thickness of the absorber layer, indicating that the performance of $MABiI_3$ will deteriorate rapidly with an increase in the thickness of the absorber layer, making it the most unstable with respect to the FF.

Among PCE in Fig. 2(d), $MASnI_3$ has the best performance at all thickness, the PCE increases rapidly in the range of 0.10 μm to 1.0 μm is from 16.66% to 29.76% while slightly decrease to 29.65% at the thickness of 1.40 μm, means this material is best suited at the thickness of near about 1 μm, but the stability issue and size of the device we optimize of $MASnI_3$ absorber at 0.80 μm. $MASnBr_3$ showing PCE increase rapidly in the range of 0.1 μm to 0.8 μm and then increases slightly. So, the PCE of $MASnBr_3$ is 24.32% at 0.80 μm, which is a good performance but still lower than $MASnI_3$. The efficiency is constant after this peak, but slightly decreases on the thicker layers. In contrast, $MABiI_3$ shows the unpreferable performance, with a maximum (23.83%) at 0.50 μm and lower efficiencies at higher thicknesses. All this indicates that $MABiI_3$ is less efficient, especially at thicker absorber layers, despite its lower Voc, Jsc, and FF. Hence, $MASnI_3$ emerges as the most favorable material among others for high-efficiency PSCs.

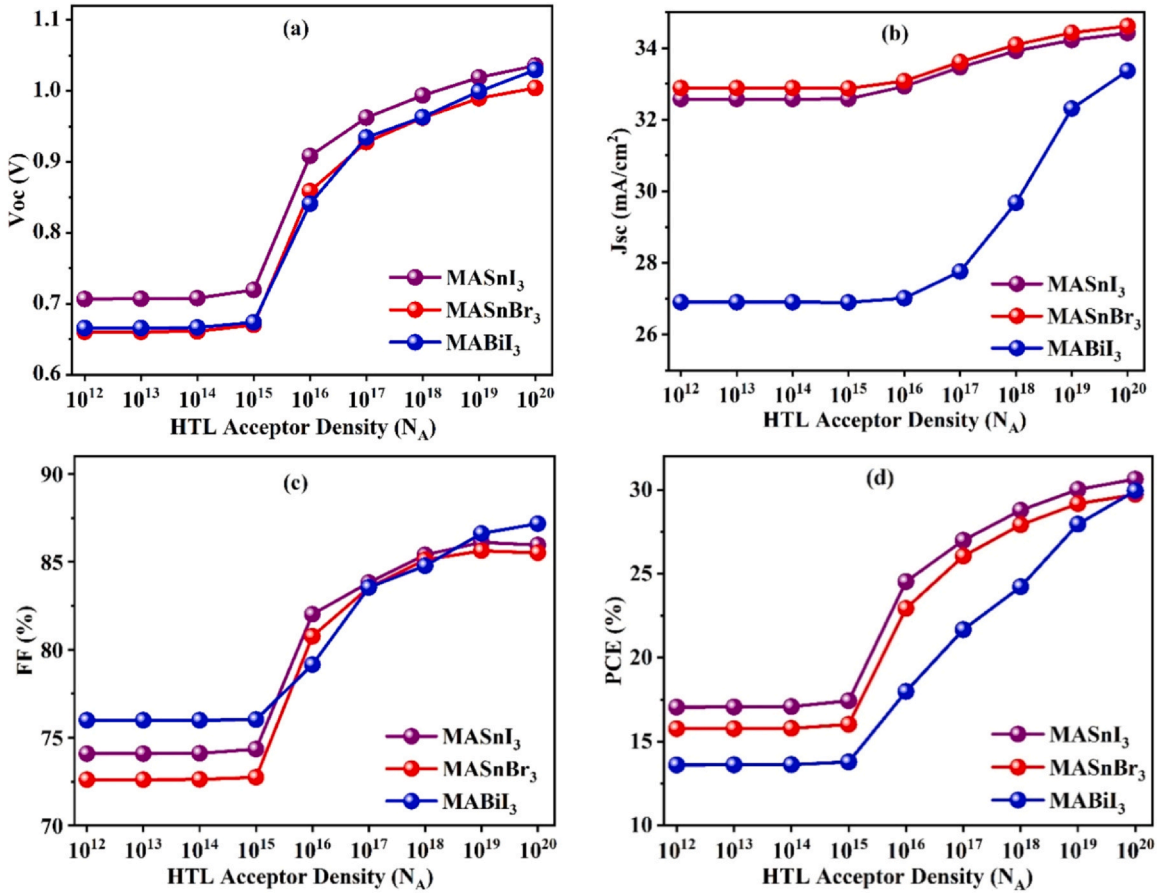

Fig. 6. Effect of variation in HTL doping concentration on (a) V_{oc}; (b) J_{sc}; (c) FF; (d) PCE. FF = fill factor; HTL = hole transport layer; J_{sc} = short-circuit current density; PCE = power conversion efficiency; V_{oc} = open-circuit voltage.

3.1.2. Optimization of acceptor density or doping concentration

The functionality of the PSC can be heavily affected by adjusting the charge transport layers (CTLs) and the perovskite material by doping [46]. At first, D1 ($MASnI_3$), D2 ($MASnBr_3$), and D3 ($MABiI_3$) devices were modeled with different acceptor densities in the perovskite absorption layer. These were 3.2×10^{15} cm^{-3}, 1×10^{18} cm^{-3}, and 3.2×10^{13} cm^{-3} respectively. Studies on the doping density effect on the performance of a PSC were simulated by varying the acceptor concentration from 10^{13} cm^{-3} to 10^{20} cm^{-3}.

Voc as a function of the Acceptor Density is depicted for the 3 absorber materials ($MASnI_3$, $MASnBr_3$, and $MABiI_3$) in Fig. 3(a), which demonstrates different trends. In $MASnI_3$, Voc increases gradually with higher acceptor density, reaching a plateau of 1.02 V at 10^{16}, and increases rapidly at higher densities from 1.02 V to 1.21 V. Voc in $MASnBr_3$ shows a steady line of 0.94 V at 10^{16} and increases up to 1.15 V after this point. The increase of Voc for $MABiI_3$ is also smaller and reaches 1.13 V at higher densities.

In Fig. 3(b), Jsc for each material is shown, showing how Jsc varies with acceptor density. For lower densities (10^{13} – 10^{16}), $MASnI_3$ shows a relatively stable Jsc of 34.37 mA/cm^2, while it starts to decrease as the density increases, which is pronounced at 10^{20}. $MASnBr_3$ begins with an even higher current density of 33.09 mA/cm^2 but experiences a gentle decline as the acceptor density increases from 10^{16}, ultimately reaching its maximum current density of 25.66 mA/cm^2 when the acceptor density is equivalent to 10^{16}. Likewise, $MABiI_3$ exhibits an overall decreasing trend for Jsc with a small maximum at 33.36 mA/cm^2 at 10^{15}, and then a gradual decline. This indicates that Jsc of $MASnI_3$ is always higher than the other 2 materials.

$MASnI_3$, the maximum FF value of 87.52% is achieved at an acceptor density of 10^{18}, followed by a slow descent in FF until reaching a plateau of ~83.10% at 10^{20}. $MASnBr_3$ depicts a similar trend, where it peaks at 84.78% at 10^{18} and declines afterward. $MABiI_3$ shows a gradual increase in FF, beginning at 80.2% at 10^{13} and reaches to 86.29% at 10^{18}, while $MASnI_3$ consistently maintains superior FF values compared to the other studied materials in Fig. 3 (c).

The plots shown in Fig. 3(d) illustrate the correlation between Acceptor Density and PCE $MASnI_3$ of 10^{16}, which presents maximum efficiency of 30.04% with only a small decrease in efficiency as this density increases. $MASnBr_3$ also achieves a maximum PCE of 25.66% at 10^{16}, and $MABiI_3$ also presents the highest PCE 25.15% at 10^{17}. The result also implies that $MASnI_3$ results in the highest PCE and shows the best potential for application in future high-efficiency lead-free PSCs. Overall, $MASnI_3$ provides the best performance on all the key parameters, including Voc, Jsc, FF, and PCE, thus a competitive material candidate for lead-free PSCs.

3.1.3. Optimization of defect density

Defect density is a key factor determining the optimal performance of the absorber layer in PSCs, since it can greatly affect carrier generation, transport, and recombination processes and embodies the quality of the entire film. Specifically, a high defect density brings about more defect states in the absorber and at the interfaces that can act as recombination centers and catalyze trap-assisted recombination

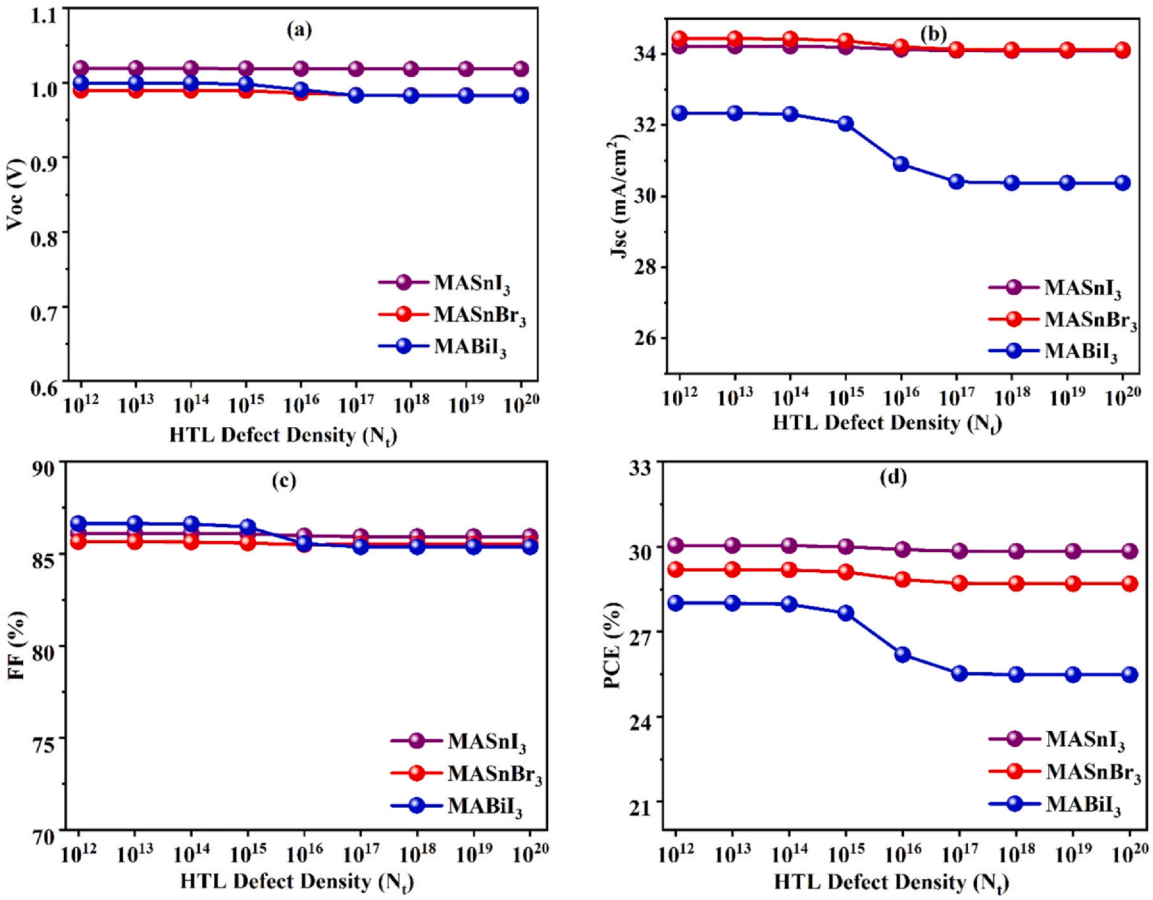

Fig. 7. Effect of variation in HTL defect density on (a) V_{oc}; (b) J_{sc}; (c) FF; (d) PCE. FF = fill factor; HTL = hole transport layer; J_{sc} = short-circuit current density; PCE = power conversion efficiency; V_{oc} = open-circuit voltage.

through the Shockley–Read–Hall channel. During this process, electrons and holes are trapped by trap states and non-radiatively recombine, which results in reduced carrier lifetime and deteriorated device performance. Low quality of the film leads to an enhancement in the density of defects [47]. The perovskite layer may contain different kinds of defects, interstitials, vacancies, Frenkel, or Schottky defects. It has been reported that the stability of PSCs was greatly impaired by the higher defect density [48]. In this work, N_t was systematically varied in the range of 10^{12} cm^{-3} to 10^{20} cm^{-3} to explore its impact on the device performance and stability of PSCs.

In Fig. 4(a) $MASnI_3$, Voc initially starts at 1.04 V at a defect density of 10^{12}, and decreases gently with increasing defect density until reaching 0.90 V at 10^{16} then decreases rapidly. This trend is also seen for $MASnBr_3$, where Voc decreases from 1.01 V at 10^{12} to 0.86 V at the level of 10^{16}. A similar pattern can be observed in $MABiI_3$ with the Voc starting at 1.01 V at 10^{12} and dropping to 0.90 V at 10^{16}. As can be seen, Voc drops for each material as defect density increases, indicative of efficiency loss from recombination at higher defect density.

Fig. 4(b) shows the dependence of Defect Density, the Jsc is steady at ~34.28 mA/cm^2 at defect density of 10^{12} to 10^{14}, and decreases gradually by increasing the defect density, reaching 16.85 mA/cm^2 at 10^{18} for $MASnI_3$. $MASnBr_3$ shows a trend paralleling this, beginning at 34.49 mA/cm^2 and dropping to 16.12 mA/cm^2 at 10^{18}. For $MABiI_3$, the trend is similar, with a decrease from 32.46 mA/cm^2 to 13.96 mA/cm^2 for 10^{18}. This means that the current density decreases with increasing defect density due to the increasing recombination rate with more defects. Similar effects were performed in $CH_3NH_3PbI_3$ [49], $CH_3NH_3SnI_3$ [50,51], and $CH_3NH_3SnBr_3$ [52]. But all absorbers show better Jsc in 10^{14}, then it dropped.

Fig. 4(c) shows $MASnI_3$, FF starts from a high value of 87.86% at the defect density 10^{12} and decreases as the defect density increases, and it falls to 53.08% at the 10^{18}. $MASnBr_3$ also exhibits a similar trend in which FF declines from 87.87% at 10^{12} to 51.47% at 10^{18}. $MABiI_3$ similarly shows a decline in FF from 87.46% to 61.34% at 10^{18}. As the defect density went up, the FF went down, which corresponds with the detrimental effects of defects on the solar cell's efficiency and performance as a whole.

The PCE for the 3 absorber materials is shown in Fig. 4(d). $MASnI_3$ has a high PCE of 31.21% at a defect density of 10^{12}, then slightly decays to 30.04% at 10^{14}, then quickly falls to 6.07% at a defect density of 10^{18}. The $MASnBr_3$ data demonstrates a similar trend; starting at 30.68% and in 10^{14} PCE is 29.19%, then decreasing to 5.29% at 10^{18}. The initial PCE of $MABiI_3$ is lower at 28.54% at 10^{12}, and it decreases to 5.76% at 10^{18}, but 27.97% in 10^{14}. Here we confirm that increasing defect density leads to a strong drop in PCE and that all 3 materials exhibit a significant drop in efficiency at increasing defect density, but all absorber are shows better PCE at defect density of 10^{14}. This emphasizes the importance of defect minimization to attain optimal performance in PSCs.

3.2. Optimization of HTL

The HTL within solar cells serves a dual function: enabling the movement of charges from the absorber to the specific electrodes and functioning as a separating layer between the absorber and the electrode [53]. The efficiency of PSCs is influenced by the impact of

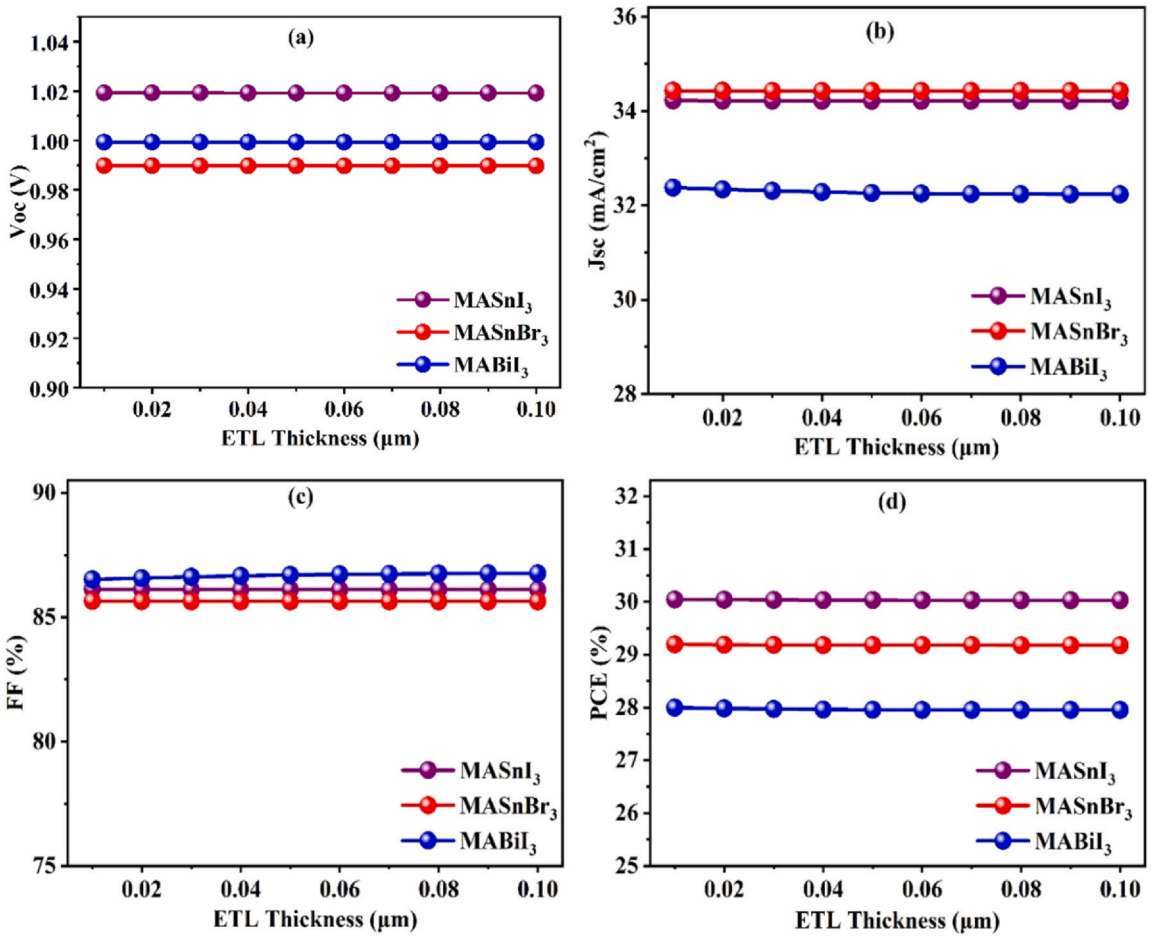

Fig. 8. Effect of ETL thickness on (a) V_{oc}; (b) J_{sc}; (c) FF, and (d) PCE. ETL = electron transport layer; FF = fill factor; J_{sc} = short-circuit current density; PCE = power conversion efficiency; V_{oc} = open-circuit voltage.

the HTL, which blocks electrons, diminishes electron-hole recombination, and aids in the migration of holes from the absorber layer to the back-contact layer [54]. To optimize PSC performance, the HTL requires a fitting band gap, positive charge carrier mobility, ideal thickness, optimal doping charge concentration, and minimal defect density.

3.2.1. *Thickness optimization of HTL*

In this investigation, the HTL employed was $CsSnI_3$, with the thickness ranging from 0.1 to 0.5 μm, aimed at analyzing its influence on perovskite structure solar cell efficiency. Fig. 5(a) indicates an Voc correlation with HTL Thickness for $MASnI_3$, $MASnBr_3$, and $MABiI_3$ absorbers with the previously noted HTLs. For $MASnI_3$, Voc is stable at 1.02 V for all HTL thicknesses from 0.05 to 0.50 μm. This implies that varying the thickness of the HTL doesn't greatly influence the Voc in $MASnI_3$. A similar trend is observed for $MASnBr_3$, where Voc does not vary within the entire range of HTL thicknesses, remaining between 0.98 V and 0.99 V. For $MABiI_3$, however, Voc increases slightly as the HTL thickness is increased from 0.98 V at 0.05 μm to 1.00 V at 0.50 μm, signifying a mild positive effect of HTL thickness on Voc for $MABiI_3$.

Fig. 5(b) displays the impact of HTL thickness on the Jsc of 3 absorbers. $MASnI_3$ and $MASnBr_3$ show almost constant current density, which is near about 34.2 mA/cm^2. $MABiI_3$ showed a similar trend, with Jsc increasing from 30.66 mA/cm^2 at 0.05 μm to 32.81 mA/cm^2 at 0.50 μm, demonstrating a direct correlation between the insertion of thicker HTL layers and the improvement in current density. The FF for all absorbers stays constant at about 86% for all HTL thicknesses, meaning that HTL thickness does not greatly affect FF, as shown in Fig. 5(c).

PCE of $MASnI_3$, rises from 29.85% for a 0.05 μm thick to 30.14% for a 0.50 μm thick HTL, resulting in a slow performed improvement in efficiency with the increase of the thickness of the HTL layers, which is illustrated in Fig. 5(d). The trend also exists for $MASnBr_3$, where PCE also increases from 28.75% (0.05 μm) to 29.36% (0.50 μm), and $MABiI_3$ shows a higher increment from 25.86% with 0.05 μm to 28.57% with 0.50 μm, confirming that thicker HTL layers can enhance $MABiI_3$ performance. So, regardless of HTL thickness, $MASnI_3$ demonstrates stable behavior with negligible alterations to Voc, Jsc, FF, and PCE.

3.2.2. *Optimization of HTL doping concentration*

The performance of the PSC device is critically dependent on the HTL, in particular, the charge carrier concentration [55]. To investigate the effect of the doping density of the HTL on the efficiency of PSCs, we studied the doping charge concentration of the acceptor (N_A) within the HTL from 10^{12} to 10^{20} cm^{-3}. Fig. 6(a) plots, Voc of $CsSnI_3$ advances from 0.71 V at a doping density of 10^{12} to fairly 1.04 V at 10^{20} for $MASnI_3$. An evident increasing trend could also be seen in Voc with increasing acceptor density, indicating a better charge separation from excitons and less recombination, which is consistent with results indicated in the literature. The same trend is observed for the Voc in $MASnBr_3$ and $MABiI_3$, where $MASnBr_3$ starts at 0.66 V at low carrier concentration and rises to 1.00 V at 10^{20}, while $CsSnI_3$ Voc trends from 0.67 V to 1.03 V over the same

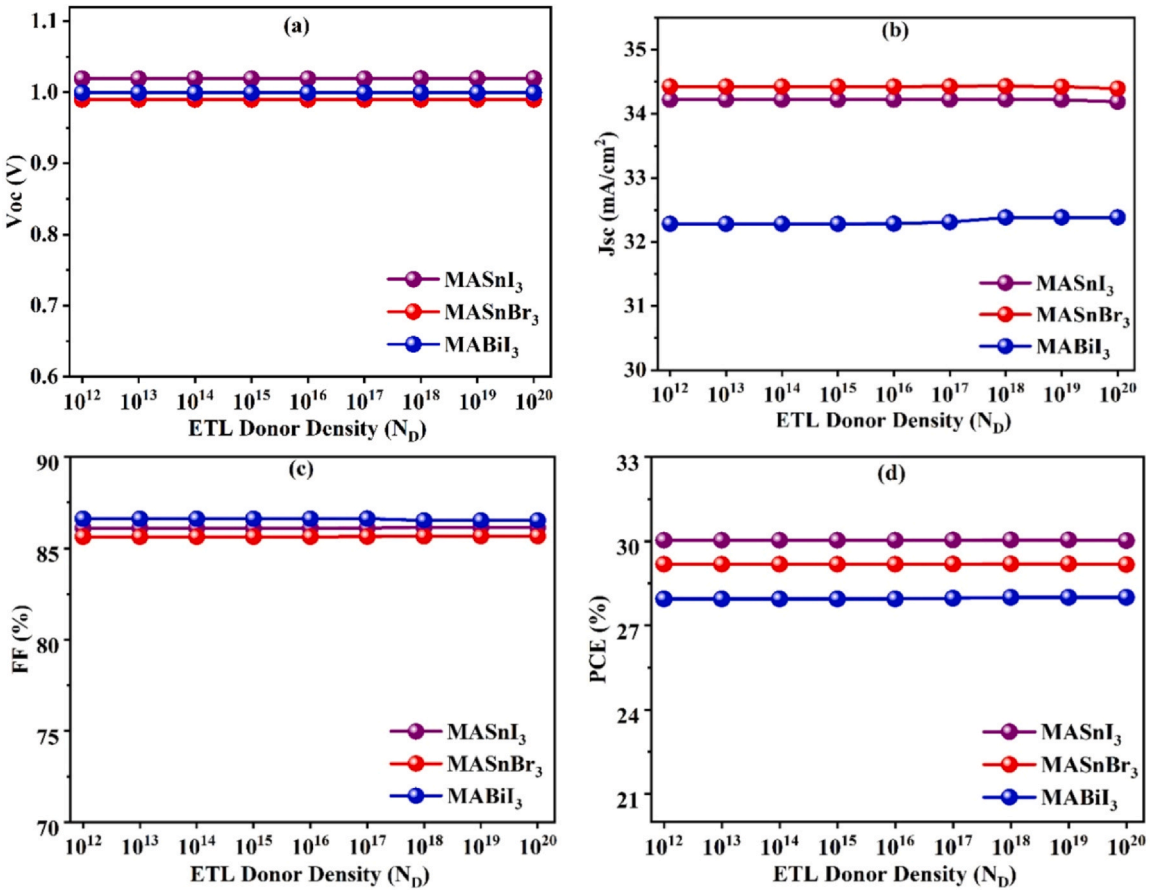

Fig. 9. Effect of ETL donor doping density on (a) V_{oc}; (b) J_{sc}; (c) FF, and (d) PCE. ETL = electron transport layer; FF = fill factor; J_{sc} = short-circuit current density; PCE = power conversion efficiency; V_{oc} = open-circuit voltage.

concentration range. These findings demonstrate that greater acceptor density leads to increased voltage per material.

For $MASnI_3$, Jsc is 32.58 mA/cm^2 with N_A is 10^{12}, and it becomes stable towards 10^{20} with a Jsc of 34.42 mA/cm^2, indicating a strong enhancement in current density with increasing acceptor density. In accordance with this trend, $MASnBr_3$ achieves 32.89 mA/cm^2 at 10^{12} and 34.62 mA/cm^2 at 10^{20}. The improvements in Jsc are most apparent for $MABiI_3$, where the Jsc improved from 26.91 mA/cm^2 to 33.36 mA/cm^2, as shown in Fig. 6(b).

FF as a function of the acceptor atoms per unit area is shown for $MASnI_3$ within shown in the lower left-hand corner of Fig. 6(c), which signifies the improvement of the overall device performance with the increase in the acceptor atoms per unit area; FF goes from 74.09% at 10^{12} to 85.97% at 10^{20}. FF is also increased from 72.61% to 85.52% in $MASnBr_3$. The FF of $MABiI_3$ was also improved, from 75.99% at 10^{12} to 87.18% at 10^{20}, confirming that higher acceptor densities also enhanced the efficiency of charge collection and FF.

In Fig. 6(d), the case of $MASnI_3$, the PCE increases linearly from 17.06% at 10^{12} to 30.65% at 10^{20}, showing a considerable improvement with increasing acceptor densities. $MASnBr_3$ also exhibits an upward trend, growing from 15.77% to 29.73%. The efficiency augmentation is most pronounced for $MABiI_3$, for which the PCE increases from 13.61% to 29.95%, indicating that a larger acceptor density is a powerful means of boosting the PCE of the solar cells. This also suggests that improvement in the performance of PSCs and deployment efficiency in practical applications requires key optimization towards acceptor density.

3.2.3. Optimization of HTL defect density

Variations in each device parameter corresponding to the defect density (N_t) within the HTL are depicted in Fig. 7 Variations in each device parameter corresponding to the defect density (N_t) within the HTL, ranging from 10^{12} cm^{-3} to 10^{20} cm^{-3}. The variation of defect density doesn't large effect on Voc and FF for all 3 absorbers, Voc and FF is 0.98 V to 1.02 V and ~86% respectively, which is shown in Fig. 7 (a) and (c).

The current density for $MASnI_3$ and $MASnBr_3$ also stays fixed for all defect density is ~34 mA/cm^2. But, $MABiI_3$ shows the Jsc is ~32 mA/cm^2 at 10^{12} to 10^{15}, then it dropped to ~30 mA/cm^2 at higher defect density, as illustrated in Fig. 7(b).

The defect density does not impact the mobility for PCE to a great extent since PCE decreases steadily from 30.04% to 29.84% (for $MASnI_3$) only until the defect density reaches 10^{20}, above which PCE remains constant. Similarly, PCE of $MASnBr_3$ also drops from 29.20% to 28.70% as defect density increases. Specifically, the PCE for $MABiI_3$ exhibits a decline from 28.01% at 10^{12} to 25.48% at 10^{20}, which signifies that defects significantly influence the performance, as shown in Fig. 7 (d).

So, higher Defect Density produces relatively small changes in Voc and FF, while Jsc and PCE decrease gradually with respect to Defect Density for each material. It also suggests that the exclusion of defects will be extremely important to enhance the performance, and particularly the PCE of PSCs.

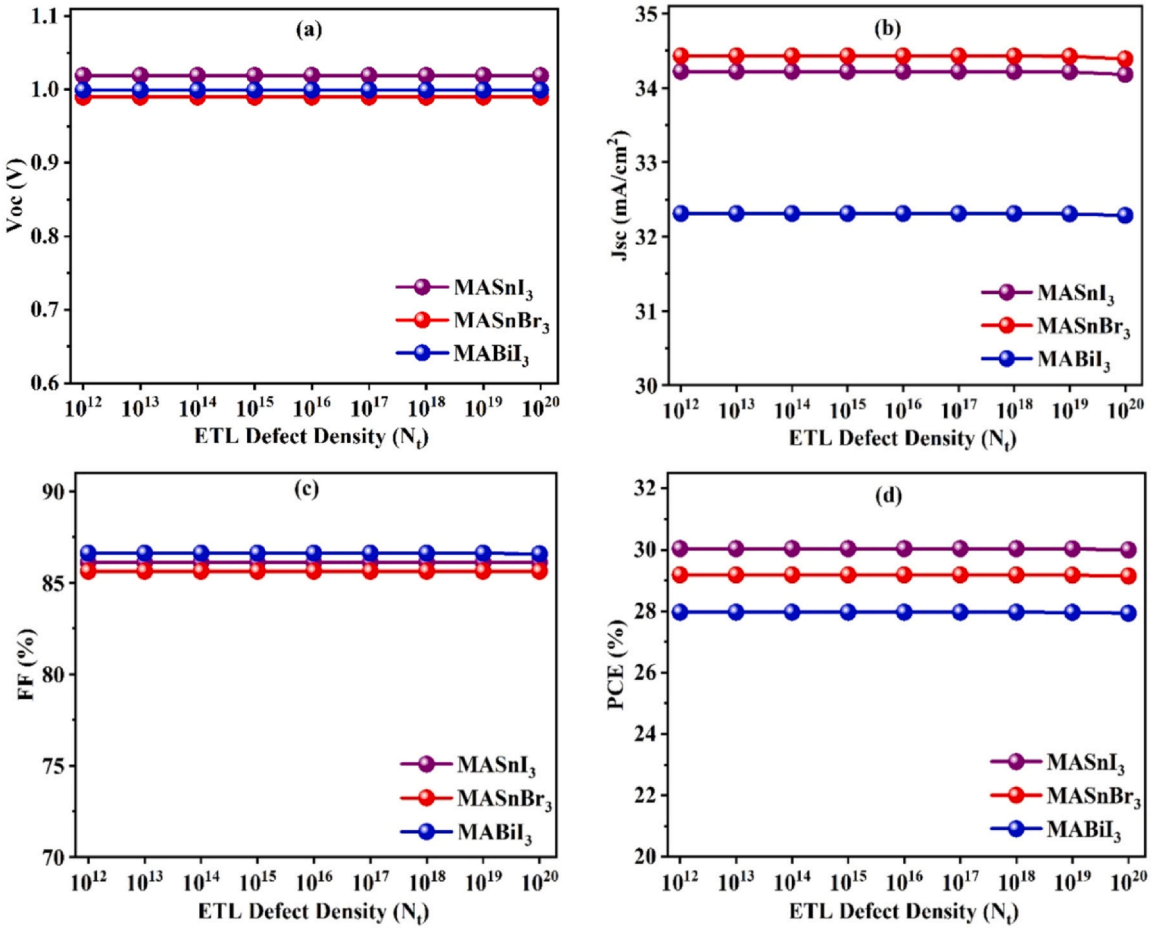

Fig. 10. Effect of ETL defect density on (a) V_{oc}; (b) J_{sc}; (c) FF, and (d) PCE. ETL = electron transport layer; FF = fill factor; J_{sc} = short-circuit current density; PCE = power conversion efficiency; V_{oc} = open-circuit voltage.

3.3. Optimization of ETL

The ETL enhances electron transfer by reducing the recombination of electron-hole pairs and obstructing the passage of light-generated holes [54]. The most effective ETL should exhibit superior electron mobility, well-suited doping levels and thickness, as well as an optimal band gap. In Figs. 8–10, try to show the variation of performance of those 3 devices with the change of thickness of ETL. But in all of the figures, there is no noticeable change in the ETL thickness. $MASnI_3$ performs much better (~30%) then other 2 absorbers $MASnBr_3$ and $MABiI_3$, which are ~29% and ~28%.

3.4. Interface defect density optimization

Defects at the interfaces of PSCs stem from mismatches in energy levels between the absorber and CTLs (including HTLs and ETLs), coupled with varying trap defect densities [56]. The escalation of interface defects amplifies trap numbers and resistance, inducing recombination and diminishing the overall cell performance [57].

Fig. 11(a-c) illustrates the relationship between Interface Defect Density and PCE for 3 different absorber and ETL configurations: $CsSnI_3/MASnI_3$, $MASnI_3/SnO_2$, $CsSnI_3/MASnBr_3$, $MASnBr_3/SnO_2$, and $CsSnI_3/MABiI_3$. For $CsSnI_3/MASnI_3$, PCE remains stable at 30.04% from 10^{10} to 10^{12}, showing minimal impact of defect density on efficiency at lower defect densities. However, as the Interface Defect Density increases beyond 10^{12}, PCE gradually decreases, dropping to 29.79% at 10^{20}, indicating that higher defect densities at the interface significantly affect performance. Similarly, $MASnI_3/SnO_2$ starts with PCE at 30.04% at 10^{10}, maintaining stable performance up to 10^{14}, but after that, PCE decreases significantly to 26.88% at $10^{20,}$ as shown in Fig. 11(a).

Fig. 11(b) shows the trend for $CsSnI_3/MASnBr_3$, where PCE begins at 29.18% and slightly decreases with increasing defect density, dropping to 28.66% at 10^{20}, showing a moderate sensitivity to interface defects. In contrast, $MASnBr_3/SnO_2$ experiences a more rapid drop, starting at 29.18% and falling to 25.90% at 10^{20}, indicating a stronger degradation in performance as interface defect density increases.

Fig. 11(c) illustrates the trend for $CsSnI_3/MABiI_3$, where PCE remains stable at 27.94% at 10^{10} and gradually decreases to 25.27% at 10^{20}, showing more gradual degradation with higher defect density. However, $MABiI_3/SnO_2$ demonstrates the most significant performance loss, with PCE decreasing from 27.94% at 10^{10} to 21.79% at 10^{20}, highlighting its higher sensitivity to interface defects.

Interface defect density significantly impacts the performance of PSCs. While $CsSnI_3/MASnI_3$ shows more stability at higher defect densities, $MASnI_3/SnO_2$ and $MABiI_3/SnO_2$ are more sensitive to interface defect density and show significant performance degradation as the defect density increases. This emphasizes the need for low-defect interfaces to ensure optimal efficiency in solar cell devices.

3.5. Metal electrode's work function optimization

For both charge extraction and transport, the interaction between the perovskite absorber and the back-contact electrode is critical to the

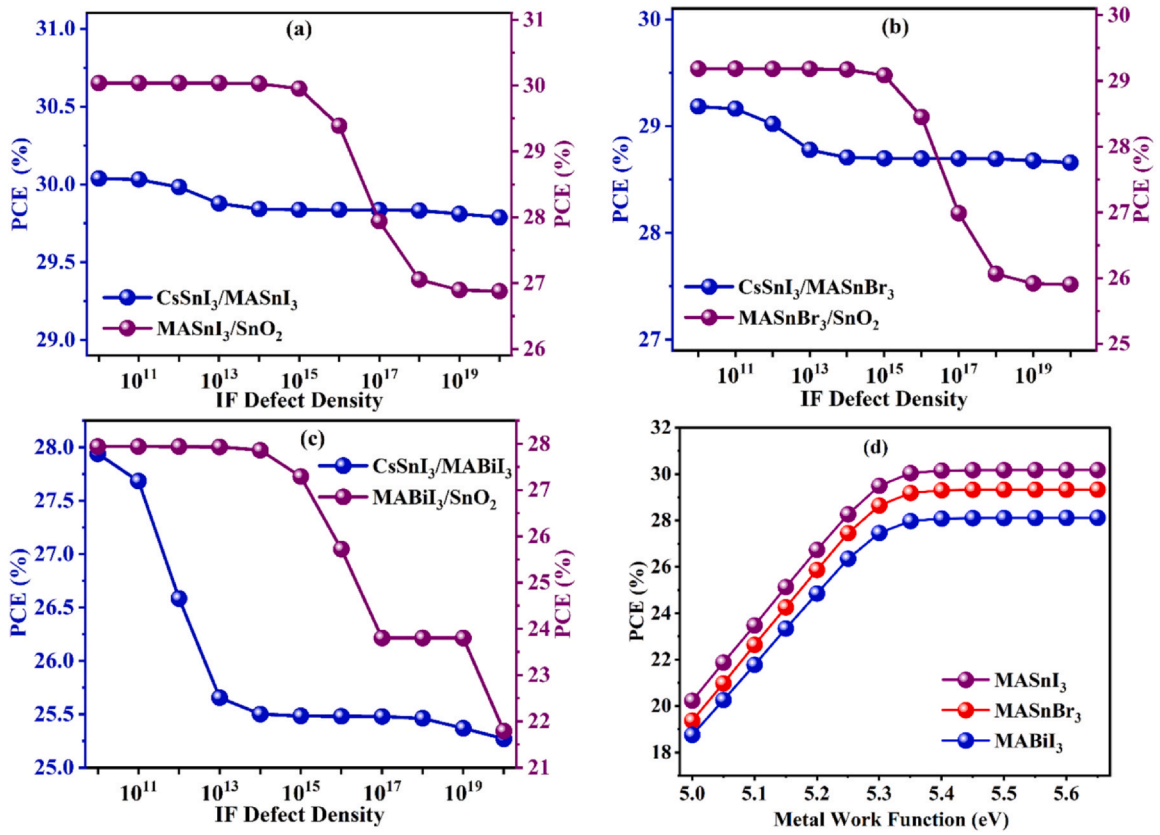

Fig. 11. (a-c) Effect of HTL/absorber and absorber/ETL interface defect density for studied compounds; (d) impact of metal work function on PV performance. ETL = electron transport layer; HTL = hole transport layer; PCE = power conversion efficiency.

efficiency of PSCs [58]. One important aspect of this alignment is the work function of the metal electrode, which is the energy needed to transfer an electron from the Fermi level of the electrode to the vacuum. Additionally, the optimal work function for PSC electrodes is between 5.0 eV and 5.65 eV, as illustrated in Fig. 11(d), providing minimal energy loss and higher efficiency [59].

Metals like Gold (Au), Carbon (C), and Tungsten (W) have work functions in this range, Nickel (Ni) with a work function of 5.35 eV is chosen for being more suitable for perovskite energy levels [60]. Nickel guarantees optimal energy level matching for maximized charge extraction efficiency and minimized metal/organic interface recombination. The mechanical stability, chemical stability, corrosion resistance, and the ability of nickel to form a stable interface with the perovskite layer make nickel ideal for long-term operation of the device.

3.6. Device performance affected via resistance

The shunt resistance (R_{sh}) and the series resistance (R_s) are the essential factors in determining the current-voltage (J-V) properties, and they greatly influence the device performances in PSCs [61]. These resistances mainly stem from layer-to-layer contacts, metal contacts, and production faults, resulting in low efficiency of the solar cell. The J-V characteristics of a hetero-junction solar cell are typically represented by the diode equation [62]:

$$J = J_L - J_0\left[\exp\left(\frac{q_e(V + JR_s)}{nK_BT}\right) - 1\right] - \frac{V + JR_s}{R_{sh}}$$

Where, J = circuit current, J_L = photocurrent generated by light absorption, V = applied voltage, and J_0 = reverse saturation current.

Both Series Resistance (Rs) and Shunt Resistance (Rsh) have a significant impact on the performance of PSCs, which can be obtained through I-V characterization of the devices. The series resistance is very crucial for the performance of the PSC. With the increasing value of Rs, the performance of the entire device degrades. The Voc and Jsc are almost unchanged with negligible alterations (~1.02 V, ~34 mA/cm^2 for $MASnI_3$, 0.99 V, ~34 mA/cm^2 for $MASnBr_3$, and 1.00 V, ~32 mA/cm^2 for $MABiI_3$), whereas FF is highly reduced as Rs increases. The FF drops from 83.16% to 65.32% with the change of Rs 1–7 Ω.cm^2 for $MASnI_3$. Same condition for $MASnBr_3$ and $MABiI_3$, FF drops down 82.42–63.84% and 83.66–66.36%, respectively (Fig. 12). This phenomenon can be observed as the filament resistance, which hinders the movement of charge carriers and leads to a reduced overall efficiency. The increasing Rs amounts yield a steadily decreasing PCE. When Rs is raised from 1 Ω·cm^2 to 7 Ω·cm^2, the absorber shows PCE decreases from 28.78% to 22.58% for $MASnI_3$, 28.10–21.75% for $MASnBr_3$, and 27.01–21.39% for $MABiI_3$. This phenomenon is mainly associated with the larger losses in the charge transport and extraction processes [63].

Conversely, shunt resistance has a detrimental impact on the PSC performance. The decline in Rsh produces an increment in the leakage current [64], which brings down PCE and FF values. For all absorbers, PCE increases when Rsh goes up from 10 Ω·cm^2 to 1 × 10^6 Ω·cm^2. Specifically, the increase in PCE for $MASnI_3$ is from 2.87% to 29.84%, $MASnBr_3$ from 2.96% to 29.19%, and $MABiI_3$ from 2.60% to 27.97%. At

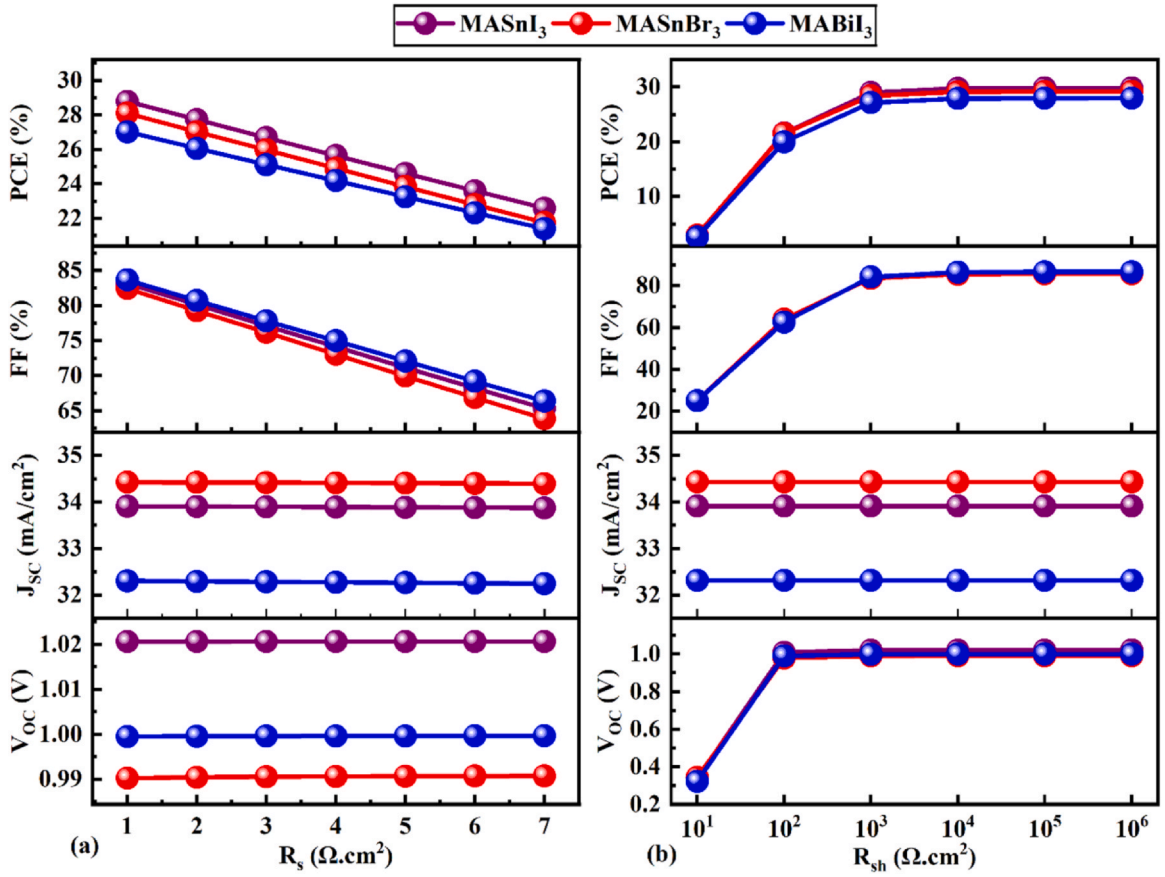

Fig. 12. Effect of a) series resistance and b) shunt resistance on: V_{oc}, J_{sc}, FF, and PCE. FF = fill factor; J_{sc} = short-circuit current density; PCE = power conversion efficiency; V_{oc} = open-circuit voltage.

higher Rsh values, this enhancement can be attributed to superior charge collection and lower recombination losses. But after 10^4, the performance of absorber are near about same, so the shunt resistance at 10^5 is more preferable.

3.7. Effect of temperature

Temperature is the underlying factor in determining the efficiency and stability of PSCs and provides valuable insight into how temperature influences device performance [65]. This decline in performance can be attributed to the elevated temperature, causing an increase in recombination rate and saturation current. For $MASnI_3$, Voc initially records at 1.02 V (300 K) and decreases to 0.89 V (400 K), while $MASnBr_3$ displays a similar initial to final decrease from 0.99 V to 0.85 V, and $MABiI_3$ decreases from 1.00 V to 0.87 V. The noted reduction in Voc directly scaled with increased temperature and can be attributed to a greater thermal energy, leading to a higher likelihood of recombination and loss of charge carriers.

Jsc does not vary significantly with temperature, $MASnI_3$ and $MASnBr_3$ present ~34 mA/cm^2, and $MABiI_3$ likewise ~32.31 mA/cm^2. Whereas Jsc is less sensitive to temperature than Voc, it still tends to decrease slightly from thermal effects on charge mobility and transport [66].

FF also drops with temperature; however, the rate of change is lower than that of Voc. For $MASnI_3$, the FF reduces from 86.12% at 300 K to 82.05% at 400 K. In contrast, for $MASnBr_3$, the FF decreases from 85.64% to 81.24%, and for $MABiI_3$, there is a drop in FF from 86.62% to 82.53%. This is apparently attributed to the higher carrier recombination and decreased overall performance of the device at higher temperatures, resulting in FF dropping.

The overall performance of devices, characterized by PCE, trends similarly down with elevated temperature. With respect to $MASnI_3$, PCE initially decreases from 30.04–24.95%, as we increase temperature from 300 K to 400 K, while for $MASnBr_3$ we observe a decrease from 29.19% to 23.83%, and for $MABiI_3$ from 27.97% to 23.27%. The reduction in PCE with temperature is due to the effects of a decreased Voc, Jsc, and a decline in FF (Fig. 13). It has been established that higher temperatures can contribute to the degradation of PSCs, where the performance of PSCs can be attributed to changes in Voc, and lesser changes in Jsc and FF under increasing temperature. This behavior can be attributed to thermal effects on carrier dynamics, recombination rates, and material properties [67].

3.8. Optimized J-V curve and quantum efficiency (QE)

Fig. 14 shows the current-voltage (J-V) curve extracted from the final PSCs modeling with 3 different absorber materials ($MASnI_3$, $MASnBr_3$, and $MABiI_3$. The figure also illustrates a comparative graphical representation of the device performance before and after optimization. We found that the device with $MASnI_3$ as the acceptor has the best performance with a Voc of 1.019 V, Jsc of 34.22 mA/cm^2, FF of 86.12%, and PCE of 30.04%. High current density and low recombination losses translate into high charge carrier collection and good device performance, as evidenced by the shape of the J-V curve. For $MASnBr_3$, the

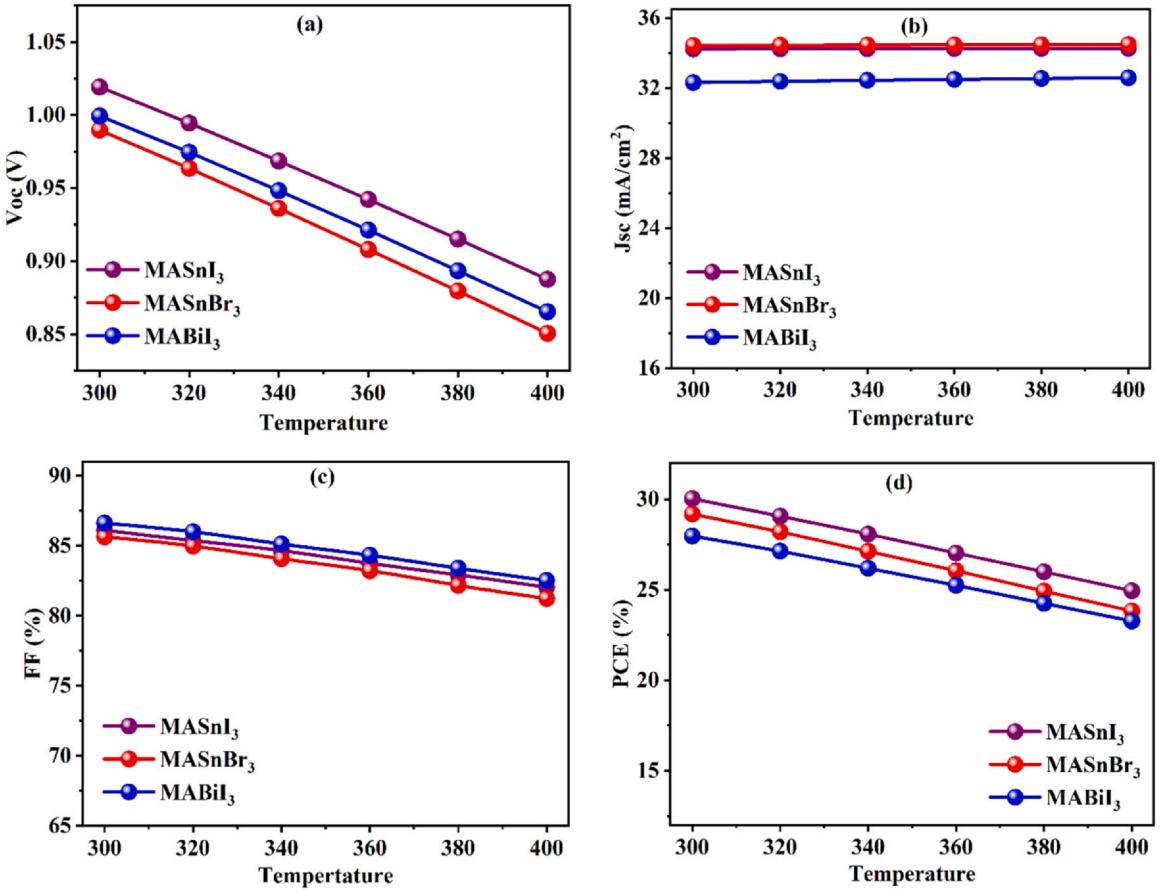

Fig. 13. Effect of temperature on: (a) V_{oc}; (b) J_{sc}; (c) FF; (d) PCE. FF = fill factor; J_{sc} = short-circuit current density; PCE = power conversion efficiency; V_{oc} = open-circuit voltage.

values are slightly lower with Voc of 0.990 V, Jsc of 34.43 mA/cm^2, FF of 85.64%, and PCE of 29.19% respectively. This lowers its efficiency relative to $MASnI_3$ because it shows a slightly lower current density and FF. $MABiI_3$ shows Voc of 0.999 V, Jsc of 32.31 mA/cm^2, FF of 86.62%, and PCE of 27.97%, reflecting a decline in performance, due to reduced current, as evidenced by the J-V curve. The relationship of the J-V curve to the performance values for the devices is obvious. The superior current and voltage characteristics of $MASnI_3$ also account for its best efficiency. On the other hand, $MABiI_3$ gives much lower current generation and conversion efficiency, which is in accordance with its overall preference in the J-V curve.

Those fig. also exhibits the efficiency of photon-to-charge conversion in each individual material over a wide wavelength range, 100–1100 nm, for all the devices associated with the research. The exponential increase observed in QE fig. is seen for all structures within the 280–360 nm range, and reached a maximum QE value of ~99.99% at 360 nm wavelength. The value is consistent along the visible region (360 nm to 780 nm), then QE gradually decreases to zero when the wavelength reaches 950 nm. QE is also dependent on the absorber thickness, as the absorber thickness increases, the QE also improves, since a thicker absorber has a greater capacity to capture photons [68]. It is important to note that the high-power conversion efficiencies (PCEs) obtained in this study represent the theoretical upper limits under idealized simulation conditions. These findings provide valuable insight into the potential of lead-free perovskite materials and offer guidance for future experimental improvements aimed at bridging the gap between theoretical predictions and real-world device performance.

3.9. Comparison with similar work

A comparative overview of various PSCs, focusing on Voc, Jsc, FF, and PCE, is illustrated in Section 3.9 (Table 3). These parameters are key indicators of the efficiency and stability of the solar uuuhe $MASnI_3$-based devices, Voc ranges from 0.87 V to 1.02 V, with the highest value of 1.019 V observed in our FTO/SnO_2/$MASnI_3$/$CsSnI_3$ configuration and Jsc for $MASnI_3$ peaks at 34.6 mA/cm^2 in the TiO_2/$MASnI_3$/2,2′,7,7′-Tetrakis(N,N-di-p-methoxyphenylamine)-9,9′-spirobifluorene structure, reflecting strong photon absorption and current generation capabilities, while $MASnBr_3$ and $MABiI_3$ exhibit comparable performance but slightly lower Jsc values (34.43 mA/cm^2 and 32.31 mA/cm^2, respectively). For FF, $MASnI_3$ achieves a maximum of 86.62% in the FTO/SnO_2/$MABiI_3$ /$CsSnI_3$ structure, indicating high charge collection efficiency, with minimal recombination losses. The PCE for $MASnI_3$-based devices reaches a peak of 30.04%, setting a new benchmark in lead-free PSC performance. This is in contrast to $MASnBr_3$ (29.19%) and $MABiI_3$ (27.97%), highlighting $MASnI_3$ as the most efficient material for these devices. The enhanced performance of $MASnI_3$ over $MASnBr_3$ and $MABiI_3$ can be ascribed to the more favorable optoelectronic properties, including higher carrier mobility, better band alignment with transport layers, and less recombination losses. The enhanced photocurrent observed in $MASnI_3$ mainly comes from the better light absorption and charge-exciton generation compared to others.

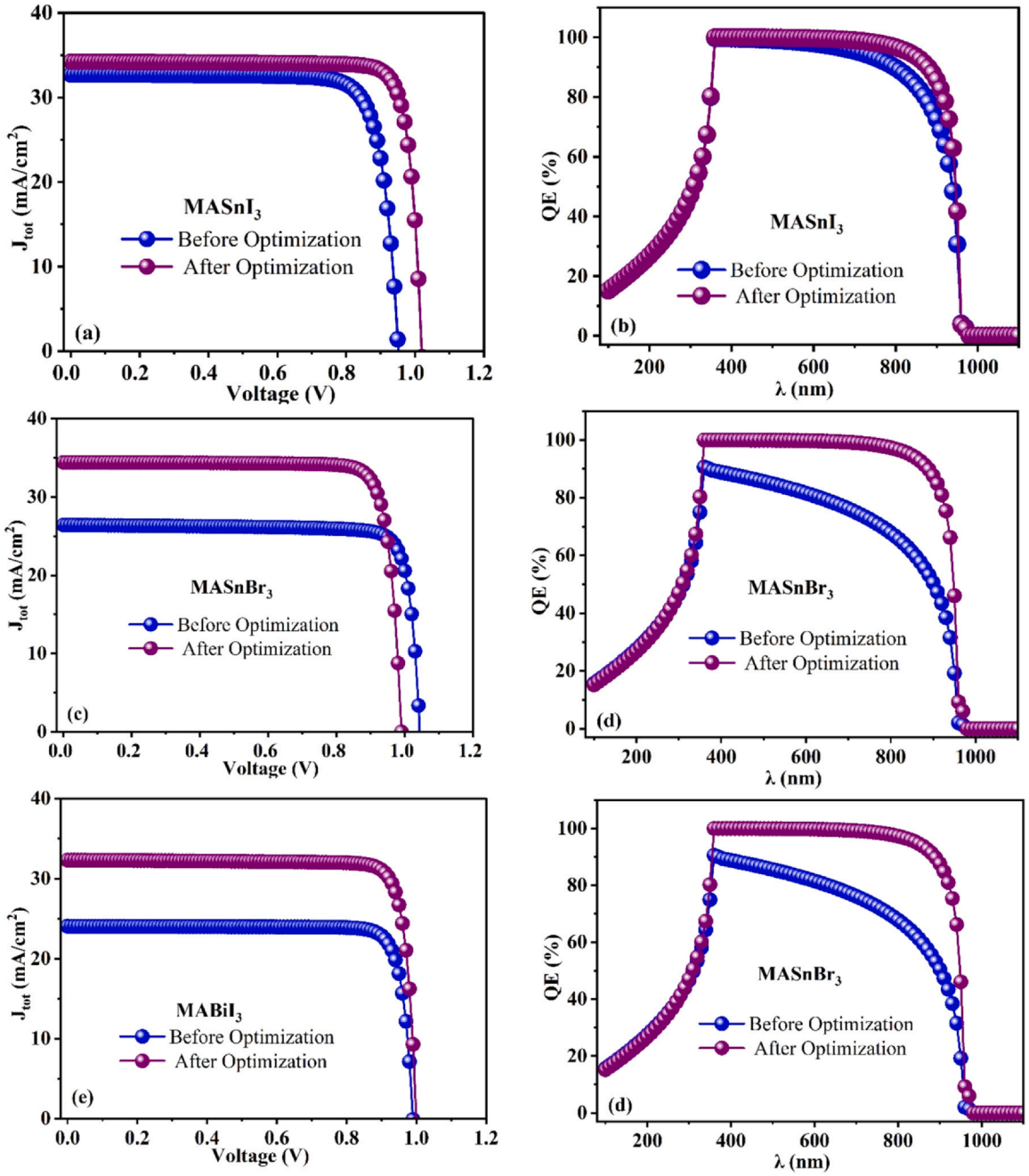

Fig. 14. Initial and final J-V curve and QE curve of 3 structures ($MASnI_3$, $MASnBr_3$, and $MABiI_3$). J-V = current-voltage; QE = quantum efficiency.

Table 3
Comparison of performance analysis with similar work

Stricture	Voc(V)	Jsc (mA/cm^2)	FF (%)	PCE (%)	Ref.
$MASnI_3$ based	0.87	33.2	78.70	23.1	[69]
ITO/PEDOT:PSS/MASnI3/PCBM/Ag	-	-	-	25.2	[70]
Al/n-MASnI3/p-Si/Au	-	-	-	27.2	[71]
TiO2/MASnI3,MASnI3/Spiro-OMeTAD	0.96	34.6	83.34	27.77	[51]
FTO/SnO_2/$MABiI_3$/$CsSnI_3$	0.99	32.31	86.62	27.97	This work
FTO/SnO2/MASnBr3 /CsSnI3	0.99	34.43	85.64	29.19	This Work
FTO/SnO_2/$MASnI_3$/$CsSnI_3$	1.019	34.22	86.11	30.04	This work

FF = fill factor; Jsc = short-circuit current density; PCE = power conversion efficiency; PEDOT:PSS = Poly(3,4-ethylenedioxythiophene):Poly(styrenesulfonate); Spiro-OMeTAD = 2,2′,7,7′-Tetrakis(N,N-di-p-methoxyphenylamine)-9,9′-spirobifluorene; Voc = open-circuit voltage.

4. Conclusions

Herein, we investigate the performance of lead-free PSCs via SCAPS-1D simulation, as well as reveal critical factors for device efficiency. The ideal thickness of the absorber layer is 800 nm for devices D1 and D2, while it is 500 nm in the case of device D3, which has a direct effect on efficiency. The best performance is achieved at a doping concentration of 10^{16} cm^{-3} for D1 and D2 and at 10^{17} cm^{-3} for D3, emphasizing the role of the density of doping layers in efficiency maximization. The higher device performance is due to lower defect densities within the perovskite absorber layer. The performance of HTL and ETL moves towards saturation with a change of thickness, while the optimized structure should be developed on the basis of the absorber layer. Furthermore, higher doping densities of the HTL lead to better device performance, and it is critical to control defect density in both HTL and ETL for device stability and efficiency. The donor doping density in the ETL is also crucial, and 10^{17} cm^{-3} gives the best performance. The study also shows that higher shunt resistance and lower series resistance are important to obtain maximum efficiency. The top performing device exhibited a Voc of over 1.019 V, Jsc of 34.22 mA/cm^2, FF of 86.116%, and a PCE of well above the 30% mark. These findings provide important insights into the design of high-efficiency lead-free PSCs and highlight the importance of material quality and performance parameters. Although the obtained efficiencies represent idealized simulation limits, the study offers practical guidance for future experimental efforts to develop stable, efficient, and environmentally friendly perovskite solar devices.

CRediT authorship contribution statement

M. A. A. Fahad: Writing – original draft, Validation, Methodology, Formal analysis, Data curation. **M. M. Islam:** Writing – original draft, Validation, Methodology, Investigation, Formal analysis, Data curation. **S. Mahmud:** Writing – review & editing, Validation, Supervision, Software, Methodology, Formal analysis, Data curation, Conceptualization. **S. Narjim:** Writing – review & editing, Visualization, Validation, Investigation. **S. Shanta:** Writing – original draft, Methodology, Investigation, Formal analysis. **M. T. Khatun:** Writing – review & editing, Validation, Investigation, Formal analysis. **M. M. Alam:** Writing – review & editing, Validation, Supervision, Project administration, Methodology, Formal analysis, Conceptualization.

Data availability

Relevant data from this study are available from the corresponding/first author upon a reasonable request.

Declaration of Competing Interest

The authors declare that they have no known competing financial interests or personal relationships that could have appeared to influence the work reported in this paper.

Acknowledgments

The authors would like to thank “Smart Computing Research Laboratory (SCRL)”, Department of EEE, Jatiya Kabi Kazi Nazrul Islam University (JKKNIU), Mymensingh-2224, Bangladesh, for providing the support needed to carry out this research.

References

[1] E.K. Oikonomou, et al., Renewable energy sources (RES) projects and their barriers on a regional scale: the case study of wind parks in the Dodecanese islands, Greece, Energy Policy 37 (11) (2009) 4874–4883, https://doi.org/10.1016/J.ENPOL.2009.06.050.

[2] N. Kannan, D. Vakeesan, Solar energy for future world: - a review, Renew. Sustain. Energy Rev. 62 (2016) 1092–1105, https://doi.org/10.1016/J.RSER.2016.05.022.

[3] Z. Şen, Solar energy in progress and future research trends, Prog. Energy Combust. Sci. 30 (4) (2004) 367–416, https://doi.org/10.1016/J.PECS.2004.02.004.

[4] E. Kabir, P. Kumar, S. Kumar, A.A. Adelodun, K.H. Kim, Solar energy: potential and future prospects, Renew. Sustain. Energy Rev. 82 (2018) 894–900, https://doi.org/10.1016/J.RSER.2017.09.094.

[5] R.R. Hernandez, et al., Environmental impacts of utility-scale solar energy, Renew. Sustain. Energy Rev. 29 (2014) 766–779, https://doi.org/10.1016/J.RSER.2013.08.041.

[6] S. Rai, B.K. Pandey, D.K. Dwivedi, Modeling of highly efficient and low cost $CH_3NH_3Pb(I_{1-x}Cl_x)_3$ based perovskite solar cell by numerical simulation, Opt. Mater. 100 (2020) 109631, https://doi.org/10.1016/J.OPTMAT.2019.109631.

[7] J.Y. Kim, J.W. Lee, H.S. Jung, H. Shin, N.G. Park, High-efficiency perovskite solar cells, Chem. Rev. 120 (15) (2020) 7867–7918, https://doi.org/10.1021/ACS.CHEMREV.0C00107.

[8] Z. Song, et al., A technoeconomic analysis of perovskite solar module manufacturing with low-cost materials and techniques, Energy Environ. Sci. 10 (6) (2017) 1297–1305, https://doi.org/10.1039/C7EE00757D.

[9] R. Sharma, A. Sharma, S. Agarwal, M.S. Dhaka, Stability and efficiency issues, solutions and advancements in perovskite solar cells: a review, Sol. Energy 244 (2022) 516–535, https://doi.org/10.1016/J.SOLENER.2022.08.001.

[10] M.A. Green, Third generation photovoltaics: solar cells for 2020 and beyond, Physica E Low-dimensional Systems Nanostructures 14 (1–2) (2002) 65–70, https://doi.org/10.1016/S1386-9477(02)00361-2.

[11] J. Yan, B.R. Saunders, Third-generation solar cells: a review and comparison of polymer:fullerene, hybrid polymer and perovskite solar cells, RSC Adv. 4 (82) (2014) 43286–43314, https://doi.org/10.1039/C4RA07064J.

[12] B. Saparov, D.B. Mitzi, Organic-inorganic perovskites: structural versatility for functional materials design, Chem. Rev. 116 (7) (2016) 4558–4596, https://doi.org/10.1021/ACS.CHEMREV.5B00715.

[13] X. Tong, F. Lin, J. Wu, Z.M. Wang, High performance perovskite solar cells, Adv. Sci. 3 (5) (2016) 1500201, https://doi.org/10.1002/ADVS.201500201.

[14] G.H. Kim, D.S. Kim, Development of perovskite solar cells with > 25% conversion efficiency, Joule 5 (5) (2021) 1033–1035, https://doi.org/10.1016/j.joule.2021.04.008.

[15] F. Wang, et al., Two-step perovskite solar cells with > 25% efficiency: unveiling the hidden bottom surface of perovskite layer, Adv. Mater. 36 (31) (2024) 2401476, https://doi.org/10.1002/ADMA.202401476.

[16] O.A. Muhammed, et al., Modeling and simulation of lead-free perovskite solar cell using SCAPS-1D, East Eur. J. Phys. 0 (2) (2021) 146–154, https://doi.org/10.26565/2312-4334-2021-2-12.

[17] M. Becker, T. Klüner, M. Wark, Formation of hybrid ABX_3 perovskite compounds for solar cell application: first-principles calculations of effective ionic radii and determination of tolerance factors, Dalton Trans. 46 (11) (2017) 3500–3509, https://doi.org/10.1039/C6DT04796C.

[18] Z. Chen, et al., Single-crystal $MAPbI_3$ perovskite solar cells exceeding 21% power conversion efficiency, ACS Energy Lett. 4 (6) (2019) 1258–1259, https://doi.org/10.1021/ACSENERGYLETT.9B00847.

[19] A.B. Coulibaly, et al., Comparative study of lead-free perovskite solar cells using different hole transporter materials, Model. Numer. Simul. Mater. Sci. 9 (4) (2019) 97–107, https://doi.org/10.4236/MNSMS.2019.94006.

[20] S. Mushtaq, et al., Performance optimization of lead-free $MASnBr_3$ based perovskite solar cells by SCAPS-1D device simulation, Sol. Energy 249 (2023) 401–413, https://doi.org/10.1016/J.SOLENER.2022.11.050.

[21] W. Fu, et al., Stability of perovskite materials and devices, Mater. Today 58 (2022) 275–296, https://doi.org/10.1016/J.MATTOD.2022.06.020.

[22] D. Kumari, N. Jaiswal, D. Punetha, S.K. Mourya, S.K. Pandey, $CsGeI_3$ perovskite-based solar cells for higher efficiency and stability: an experimental investigation, IEEE J. Photovolt. 15 (4) (2025) 533–540, https://doi.org/10.1109/JPHOTOV.2025.3563882.

[23] M. Chen, et al., Highly stable and efficient all-inorganic lead-free perovskite solar cells with native-oxide passivation, *10:1*, Nat. Commun. 2019 10 (1) (2019) 16, https://doi.org/10.1038/s41467-018-07951-y.

[24] C.N. Savory, A. Walsh, D.O. Scanlon, Can Pb-free halide double perovskites support high-efficiency solar cells? ACS Energy Lett. 1 (5) (2016) 949–955, https://doi.org/10.1021/ACSENERGYLETT.6B00471.

[25] K. Nishimura, et al., Lead-free tin-halide perovskite solar cells with 13% efficiency, Nano Energy 74 (2020) 104858, https://doi.org/10.1016/J.NANOEN.2020.104858.

[26] S. Shao, M.A. Loi, S. Shao, O.A.L. Photophysics, The role of the interfaces in perovskite solar cells, Adv. Mater. Interfaces 7 (1) (2020) 1901469, https://doi.org/10.1002/ADMI.201901469.

[27] W. Chi, S.K. Banerjee, StabIlity improvement of perovskite solar cells by compositional and interfacial engineering, Chem. Mater. 33 (5) (2021) 1540–1570, https://doi.org/10.1021/ACS.CHEMMATER.0C04931.

[28] G. Ren, et al., Strategies of modifying spiro-OMeTAD materials for perovskite solar cells: a review, J. Mater. Chem. A 9 (8) (2021) 4589–4625, https://doi.org/10.1039/D0TA11564A.

[29] L. Hu, et al., PEDOT:PSS monolayers to enhance the hole extraction and stability of perovskite solar cells, J. Mater. Chem. A 6 (34) (2018) 16583–16589, https://doi.org/10.1039/C8TA05234D.

[30] K.P. Marshall, M. Walker, R.I. Walton, R.A. Hatton, Enhanced stability and efficiency in hole-transport-layer-free $CsSnI_3$ perovskite photovoltaics, Nat. Energy 1 (12) (2016) 1–9, https://doi.org/10.1038/NENERGY.2016.178.

[31] M. Atowar Rahman, Enhancing the photovoltaic performance of Cd-free Cu_2ZnSnS_4 heterojunction solar cells using SnS HTL and TiO_2 ETL, Sol. Energy 215 (2021) 64–76, https://doi.org/10.1016/J.SOLENER.2020.12.020.

[32] M.M. Tavakoli, P. Yadav, R. Tavakoli, J. Kong, Surface engineering of TiO_2 ETL for highly efficient and hysteresis-less planar perovskite solar cell (21.4%) with enhanced open-circuit voltage and stability, Adv. Energy Mater. 8 (23) (2018) 1800794, https://doi.org/10.1002/AENM.201800794.

[33] Q. Jiang, X. Zhang, J. You, SnO_2: a wonderful electron transport layer for perovskite solar cells, Small 14 (31) (2018) 1801154, https://doi.org/10.1002/SMLL.201801154.

[34] S. Bansal, P. Aryal, Evaluation of new materials for electron and hole transport layers in perovskite-based solar cells through SCAPS-1D simulations (November), Conf. Rec. IEEE Photovolt. Spec. Conf. 2016 (2016) 747–750, https://doi.org/10.1109/PVSC.2016.7749702.

[35] M. Ismail, M. Noman, S. Tariq Jan, M. Imran, Boosting efficiency of eco-friendly perovskite solar cell through optimization of novel charge transport layers, R. Soc. Open Sci. 10 (6) (2023) 230331, https://doi.org/10.1098/RSOS.230331.

[36] I. Elango, M. Selvamani, P.C. Ramamurthy, A.V. Kesavan, Studying V_{OC} in lead free inorganic perovskite photovoltaics by tuning energy bandgap and defect density, Ceram. Int. 48 (19) (2022) 29414–29420, https://doi.org/10.1016/J.CERAMINT.2022.06.125.

[37] F. Jannat, S. Ahmed, M.A. Alim, Performance analysis of cesium formamidinium lead mixed halide based perovskite solar cell with MoOx as hole transport material via SCAPS-1D, Optik 228 (2021) 166202, https://doi.org/10.1016/J.IJLEO.2020.166202.

[38] H.-J. Du, W.-C. Wang, J.-Z. Zhu, Device simulation of lead-free $CH_3NH_3SnI_3$ perovskite solar cells with high efficiency*, Chin. Phys. B 25 (10) (2016) 108802, https://doi.org/10.1088/1674-1056/25/10/108802.

[39] A.K. Al-Mousoi, et al., Simulation and analysis of lead-free perovskite solar cells incorporating cerium oxide as electron transporting layer, RSC Adv. 12 (50) (2022) 32365–32373, https://doi.org/10.1039/D2RA05957F.

[40] K.H. Mahmoud, A.S. Alsubaie, A.H. Anwer, M.Z. Ansari, Comparative analysis of perovskite solar cells for obtaining a higher efficiency using a numerical approach, *Vol. 14, Page 1127*, Micromachines 2023 14 (6) (2023) 1127, https://doi.org/10.3390/MI14061127.

[41] A.A. Goje, et al., Design and simulation of lead-free flexible perovskite solar cell using SCAPS-1D, IOP Confer. Ser. Mater. Sci. Eng. 1278 (1) (2023) 012004, https://doi.org/10.1088/1757-899X/1278/1/012004.

[42] S. Mushtaq, et al., Performance optimization of lead-free $MASnBr_3$ based perovskite solar cells by SCAPS-1D device simulation, in: S. ElsevierS Mushtaq, A. Tahir, R.S. Ashfaq, M. Bonilla, R. Haneef, W. Saeed, N. Ahmad (Eds.), AminSolar Energy, Elsevier, 2023, ⟨https://www.sciencedirect.com/science/article/pii/S0038092X22008702⟩ Accessed: Mar. 07, 2025. [Online]. Available.

[43] M. Wahid, U. Das, B. Paul, S. Paul, … M.H.-M.S.., and undefined 2023, Numerical simulation for enhancing performance of MoS_2 hetero-junction solar cell employing Cu2O as hole transport layer academia.eduMF Wahid, U Das, BK Paul, S Paul, MN Howlader, MS RahmanMater. Sci. Appl, 2023•academia.edu, Accessed: Apr. 06, 2026. [Online]. Available: ⟨https://www.academia.edu/download/117828981/PaperDownload.pdf⟩.

[44] A. Hima, N. Lakhdar, B. Benhaoua, A. Saadoune, I. Kemerchou, F. Rogti, An optimized perovskite solar cell designs for high conversion efficiency, Superlattices Microstruct. 129 (2019) 240–246, https://doi.org/10.1016/J.SPMI.2019.04.007.

[45] O.D. Iakobson, O.L. Gribkova, A.R. Tameev, J.M. Nunzi, A common optical approach to thickness optimization in polymer and perovskite solar cells, Mar. 2021, Sci. Rep. 11 (1) (2021) 1–6, https://doi.org/10.1038/s41598-021-84452-x.

[46] M. Tahir, et al., Praseodymium doped nickel oxide as hole-transport layer for efficient planar Perovskite Solar Cells, Optik 300 (2024) 171630, https://doi.org/10.1016/J.IJLEO.2024.171630.

[47] T.S. Sherkar, et al., Recombination in perovskite solar cells: significance of grain boundaries, interface traps, and defect ions, ACS Energy Lett. 2 (5) (2017) 1214–1222, https://doi.org/10.1021/ACSENERGYLETT.7B00236.

[48] J. Zhang, W. Zhao, S. Olthof, S. Liu, Defects in $CsPbX_3$ perovskite: from understanding to effective manipulation for high-performance solar cells, Small Methods 5 (11) (2021) 2100725, https://doi.org/10.1002/SMTD.202100725.

[49] M.S. Jamal, et al., Effect of defect density and energy level mismatch on the performance of perovskite solar cells by numerical simulation, Optik 182 (2019) 1204–1210, https://doi.org/10.1016/J.IJLEO.2018.12.163.

[50] M. Shah, et al., Utilizing density functional theory and SCAPS simulations for modeling high-performance $MASnI_3$-based perovskite solar cells, Energy Technol. 12 (3) (2024) 2301228, https://doi.org/10.1002/ENTE.202301228.

[51] H. Mouhib, et al., Numerical investigation of eco-friendly $MASnI_3$ perovskite-based solar cell: effect of defect density and hole transport layer, Model. Simul. Mater. Sci. Eng. 30 (3) (2022) 035011, https://doi.org/10.1088/1361-651X/AC55B0.

[52] M. Shah, et al., First-Principles insights and SCAPS-1D simulations for optimizing $MASnBr_3$-based perovskite solar cells, Comput. Mater. Sci. 250 (2025) 113699, https://doi.org/10.1016/J.COMMATSCI.2025.113699.

[53] H.J. An, S.D. Baek, D.H. Kim, J.M. Myoung, Energy and charge dual transfer engineering for high-performance green perovskite light-emitting diodes, Adv. Funct. Mater. 32 (21) (2022) 2112849, https://doi.org/10.1002/ADFM.202112849.

[54] F. Azri, A. Meftah, N. Sengouga, A. Meftah, Electron and hole transport layers optimization by numerical simulation of a perovskite solar cell, Sol. Energy 181 (2019) 372–378, https://doi.org/10.1016/J.SOLENER.2019.02.017.

[55] A. Bag, R. Radhakrishnan, R. Nekovei, R. Jeyakumar, Effect of absorber layer, hole transport layer thicknesses, and its doping density on the performance of perovskite solar cells by device simulation, Sol. Energy 196 (2020) 177–182, https://doi.org/10.1016/J.SOLENER.2019.12.014.

[56] A.S. Chouhan, N.P. Jasti, S. Avasthi, Effect of interface defect density on performance of perovskite solar cell: Correlation of simulation and experiment, Mater. Lett. 221 (2018) 150–153, https://doi.org/10.1016/J.MATLET.2018.03.095.

[57] S. Tariq Jan, M. Noman, Influence of layer thickness, defect density, doping concentration, interface defects, work function, working temperature and reflecting coating on lead-free perovskite solar cell, Sol. Energy 237 (2022) 29–43, https://doi.org/10.1016/J.SOLENER.2022.03.069.

[58] C.K. Chung, W.T. Chang, R.X. Zhou, Effect of cobalt content on the work function of the electrodeposited nickel-cobalt films, Microsyst. Technol. 14 (9–11) (2008) 1389–1394, https://doi.org/10.1007/S00542-007-0502-2/METRICS.

[59] M.I. Hossain, B. Aïssa, Effect of structure, temperature, and metal work function on performance of organometallic perovskite solar cells, J. Electron. Mater. 46 (3) (2017) 1806–1810, https://doi.org/10.1007/S11664-016-5232-8/METRICS.

[60] K.H. Kim, D. Brunel, A. Gohier, L. Sacco, M. Châtelet, C.S. Cojocaru, Cup-stacked carbon nanotube schottky diodes for photovoltaics and photodetectors, Adv. Mater. 26 (25) (2014) 4363–4369, https://doi.org/10.1002/ADMA.201400775.

[61] M.K. Hossain, M.H.K. Rubel, G.F.I. Toki, I. Alam, M.F. Rahman, H. Bencherif, Effect of various electron and hole transport layers on the performance of $CsPbI_3$-based perovskite solar cells: a numerical investigation in DFT, SCAPS-1D, and wxAMPS frameworks, ACS Omega 7 (47) (2022) 43210–43230, https://doi.org/10.1021/ACSOMEGA.2C05912.

[62] D.K. Maram, H. Abnavi, H. Habibiyan, H. Ghafoorifard, O. Shekoofa, TDMA based numerical approach on modeling of charge carrier transport and ion vacancy motion in perovskite solar cells, 28th Iran. Conf. Electr. Eng. (ICEE) 2020 (2020) 1–7.

[63] S. Wang, et al., Impact of loss mechanisms on performances of perovskite solar cells, Physica B Condensed Matter 647 (2022) 414363, https://doi.org/10.1016/J.PHYSB.2022.414363.

[64] G. Şahin, M. Hakkı Alma, Study of the static characteristic I-V and the electrical parameters corresponding to the shunt resistance Rsh and series resistance Rs per unit area of a solar cell with grain size, Chin. J. Phys. 62 (2019) 395–404, https://doi.org/10.1016/J.CJPH.2019.09.034.

[65] I. Mesquita, L. Andrade, A. Mendes, Temperature impact on perovskite solar cells under operation, ChemSusChem 12 (10) (2019) 2186–2194, https://doi.org/10.1002/CSSC.201802899.

[66] A.D. Sheikh, et al., Effects of high temperature and thermal cycling on the performance of perovskite solar cells: acceleration of charge recombination and deterioration of charge extraction, ACS Appl. Mater. Interfaces 9 (40) (2017) 35018–35029, https://doi.org/10.1021/acsami.7b11250.

[67] T.J. Savenije, J.E. Kroeze, X. Yang, J. Loos, The effect of thermal treatment on the morphology and charge carrier dynamics in a polythiophene–fullerene bulk heterojunction, Adv. Funct. Mater. 15 (8) (2005) 1260–1266, https://doi.org/10.1002/ADFM.200400559.

[68] K.K. Mamta, V.N. Maurya, Singh, Sb_2Se_3/CZTS dual absorber layer based solar cell with 36.32% efficiency: a numerical simulation, J. Sci. Adv. Mater. Dev. 7 (2) (2022) 100445, https://doi.org/10.1016/J.JSAMD.2022.100445.

[69] R. Sahani, S.K. Pandey, A comparative study of different $MASnI_3$-based perovskite solar cells to identify an optimized and stable PSC structure, *54:10*, J. Electron. Mater. 54 (10) (2025) 8732–8744, https://doi.org/10.1007/S11664-025-12229-3.

[70] D. Bai, et al., $ASnX_3$—better than Pb-based perovskite, Nano Sel. 2 (2) (2021) 159–186, https://doi.org/10.1002/NANO.202000172.

[71] C. Yadav, S. Kumar, Numerical simulation of lead-free $MASnI_3$ perovskite/silicon heterojunction for solar cells and photodetectors, Results Surf. Interfaces 17 (2024) 100301, https://doi.org/10.1016/J.RSURFI.2024.100301.